CANCER

BCL-X_L–targeting antibody-drug conjugates are active in preclinical models and mitigate on-mechanism toxicity of small-molecule inhibitors

Andrew S. Judd, Bhupinder Bawa, Wayne R. Buck, Zhi-Fu Tao, Yingchun Li, Michael J. Mitten†, Milan Bruncko, Nathaniel Catron, George Doherty, Kenneth R. Durbin†, Brian Enright, Robin Frey, Deanna Haasch, Sandra Haman†, Anthony R. Haight†, Tracy A. Henriques, James Holms†, Kamel Izeradjene, Russell A. Judge, Gary J. Jenkins, Aaron Kunzer, Joel D. Leverson†, Ruth L. Martin, Diya Mitra, Scott Mittelstadt, Lorne Nelson, Paul Nimmer†, Joann Palma, Richard Peterson, Darren C. Phillips, Sherry L. Ralston, Saul H. Rosenberg†, Xiaoqiang Shen, Xiaohong Song, Kedar S. Vaidya†, Xilu Wang, Jin Wang, Yu Xiao, Haichao Zhang, Xinxin Zhang, Eric A. Blomme, Erwin R. Boghaert†, John C. Kalvass, Andrew Phillips, Andrew J. Souers*

Overexpression of the antiapoptotic protein B-cell lymphoma-extra large (BCL-X_L) is associated with drug resistance and disease progression in numerous cancers. The compelling nature of this protein as a therapeutic target prompted efforts to develop selective small-molecule BCL-X_L inhibitors. Although efficacious in preclinical models, we report herein that selective BCL-X_L inhibitors cause severe mechanism-based cardiovascular toxicity in higher preclinical species. To overcome this liability, antibody-drug conjugates were constructed using altered BCL-X_L–targeting warheads, unique linker technologies, and therapeutic antibodies. The epidermal growth factor receptor–targeting antibody-drug conjugate AM1-15 inhibited growth of tumor xenografts and did not cause cardiovascular toxicity nor dose-limiting thrombocytopenia in monkeys. While an unprecedented BCL-X_L–mediated toxicity was uncovered in monkey kidneys upon repeat dosing of AM1-15, this toxicity was mitigated via further drug-linker modification to afford AM1-AAA (AM1-25). The AAA drug-linker has since been incorporated into mirzotamab clezutoclax, the first selective BCL-X_L–targeting agent to enter human clinical trials.

INTRODUCTION

Dysregulated apoptosis is a hallmark of tumorigenesis and is often associated with the overexpression of prosurvival members of the B-cell lymphoma-2 (BCL-2) protein family (*1*, *2*), most notably BCL-2, BCL-X_L, and myeloid cell leukemia-1 (MCL-1). High expression of BCL-2 is predominantly associated with increased resistance to apoptosis in hematologic malignancies (*3*). The related protein BCL-X_L is the primary survival factor in multiple solid and some hematologic tumors (*4*, *5*). Navitoclax, an orally bioavailable inhibitor of both BCL-2 and BCL-X_L (*6*, *7*), was the first BCL-2 family inhibitor to show clinical activity (*8*, *9*). As predicted by preclinical data (*10*), systemic inhibition of BCL-X_L with navitoclax induces a rapid, concentration-dependent decrease in circulating platelets. This mechanism-based thrombocytopenia is the predominant dose-limiting toxicity of single-agent navitoclax treatment (*8*, *9*, *11*) in patients. While this toxicity led to the design and subsequent approval of the BCL-2–selective and platelet-sparing inhibitor venetoclax (*12*), appropriate entry criteria, scheduling, and choice of combination partners have allowed for management of thrombocytopenia and progression of navitoclax into additional ongoing clinical trials (*13*, *14*).

In early clinical investigations in patients with solid tumors, the combination of navitoclax with various chemotherapeutic regimens produced greater neutropenia than expected from chemotherapy alone (*15*). This limited the ability to achieve optimal exposures and, hence, efficacy of these navitoclax-based regimens. Highly potent, selective, and orally bioavailable BCL-X_L small-molecule inhibitors (SMIs) were therefore generated (*16*, *17*) and used to determine that (i) the preclinical combination activity of navitoclax in solid tumor models was largely driven by BCL-X_L inhibition and (ii) the neutropenia caused by navitoclax was driven by BCL-2 inhibition (*16*). However, we report here that, in addition to the expected thrombocytopenia, highly selective BCL-X_L SMIs cause rapid and severe cardiovascular toxicity in higher preclinical species that is mechanism-based, thus precluding their development as systemically delivered SMI agents. This discovery was particularly unexpected, given the lack of cardiovascular toxicity observed with navitoclax in preclinical studies or human clinical trials (*18*).

Because of the potential of BCL-X_L inhibitors to treat various cancers (*16*), we proposed that an antibody-drug conjugate (ADC) approach could offer a means of selectively targeting this protein in cancer cells while circumventing the mechanism-based toxicity (*19*) of systemically available SMIs. Multiple ADCs have been evaluated for antitumor activity in the clinic, with several successful examples (*20*). However, all have cytotoxic payloads that affect malignant and normal tissues with minimal discrimination; consequently, nonspecific ADC uptake and released "free" circulating payload typically limit the doses of these ADCs that can be safely administered (*21*, *22*). Our studies with BCL-X_L SMIs indicated that a limited number of tissues were adversely affected by compound treatment, whereas most organs were not affected. Therefore, we investigated whether an ADC targeting an antigen expressed on

AbbVie Inc., 1 N. Waukegan Road, North Chicago, IL 60064, USA.
*Corresponding author. Email: andrew.souers@abbvie.com
†Retired.

tumors but not on BCL-X_L–dependent normal tissues would enable an enhanced therapeutic index (TI) relative to BCL-X_L SMIs and ADCs containing broadly cytotoxic payloads.

ADC payload, linker, and antibody attachment technologies have historically been developed to facilitate the utility of natural product–derived cytotoxins (*23*) which, in general, have favorable chemical properties relative to the large, hydrophobic, and typically insoluble BCL-2 family inhibitors (*24*). In the course of our efforts to bring among the first targeted-payload ADCs to patients with cancer, we found that technology development was required to enable the generation of BCL-X_L payload-based conjugates with drug-like properties. Extensive modifications and robust toxicological investigations ultimately afforded drug-linker 25. Conjugation of 25 to an epidermal growth factor receptor (EGFR)–targeting antibody afforded ADC AM1-25, which demonstrated robust antitumor activity in vivo and a substantially improved TI with respect to thrombocytopenia and cardiovascular safety in animals. The generation of this drug-linker technology, along with the data described herein, provides the seminal example of a BCL-X_L payload-based ADC for cancer therapy. Last, the described AAA drug-linker has since been incorporated into mirzotamab clezutoclax (*25*), which is the first selective BCL-XL–targeting agent to be evaluated in human patients (NCT03595059).

RESULTS

Potent, selective BCL-X_L inhibitors cause on-target cardiovascular toxicity in dogs

As previously reported, the potent and selective BCL-X_L inhibitor A-1331852 (1) caused rapid thrombocytopenia in rodents and inhibited growth of xenografts of human tumors in mice (*16*, *17*). During the first evaluation of pharmacokinetic properties of A-1331852 in dogs, groups of three dogs each received intravenous or oral doses (2.5 mg/kg). Two hours after intravenous dosing, dogs developed ataxia and recumbency, progressing within 15 min to weak pulse, cyanosis (SaO_2 ~ 90%), and death or euthanasia despite supportive care (oxygen and fluid therapy). Orally dosed dogs followed a similar course, delayed 45 min relative to intravenous dosing. Gross findings of hydropericardium and pulmonary congestion were seen in all dogs; two dogs had perivascular pulmonary hemorrhage. Thrombocytopenia (as low as 5000 platelets/μl, normal >200,000/μl), hemoconcentration (hematocrit of 54 to 68%), hypoalbuminemia, and alkalosis were also observed in all treated dogs. The mean maximum compound concentrations measured in intravenous and oral groups were 26.5 (6 min) and 3.0 (2 hours) μg/ml, respectively (table S1). Given the tolerability of A-1331852 in rodents (*16*) and the general safety of navitoclax across species (*6*), the toxicity observed in dogs was unexpected. On the basis of the rapid occurrence of the described effects, we speculated that A-1331852 was adversely affecting cardiovascular function.

To challenge this postulate, we administered A-1331852 as an intravenous bolus (2-min infusion) into the femoral vein of two anesthetized and instrumented dogs (*26*). In addition to multiple indices of cardiovascular function and platelet numbers, markers of platelet activation and cytokine release were also assessed to examine potential roles in the toxicity. Approximately 60 min into the experiment, a decrease in mean arterial pressure (MAP) was observed; MAP continued to decline rapidly (Fig. 1A) to the point where both dogs reached a MAP of 50 mmHg (approximately 65 to 85 min) after which the experiment was terminated. Heart rate showed a concomitant and precipitous decline, along with the other cardiovascular parameters (fig. S1). A gross alteration in waveform and amplitude of the QRS complex was observed in the lead II electrocardiogram and in a time frame that only preceded the deterioration of MAP (Fig. 1A, right, and fig. S1, respectively).

Gross findings were limited to hydropericardium (<10 ml), which coagulated on exposure to air, and an edematous heart. Morphologic changes of the heart as assessed by histopathology included interstitial myocardial edema and diffuse pyknosis of myocardial capillary endothelium that spared larger vessels (Fig. 1B). Immunohistochemistry (IHC) for activated caspase-3 confirmed diffuse (essentially 100%) capillary endothelial apoptotic cell death within the myocardium (Fig. 1B). Subsequent electron microscopic examination of myocardium demonstrated nuclear pyknosis that was limited to capillary endothelial cells. Ultrastructurally, cardiomyocytes had minimal intracellular edema without any nuclear or mitochondrial changes (Fig. 1C). Platelet count decreased below 10,000/μl within 30 min of dosing (Fig. 1D), which was consistent with the identified pulmonary hemorrhage.

Cytokines were profiled, given a possible role in driving endothelial injury through an indirect mechanism, which might have accounted for the 2-hour delay from dose administration to endothelial injury. Interleukin-10 (IL-10), an endothelial protective factor (*27*), was decreased to less than 10% of baseline in parallel with platelet decreases and well ahead of cardiovascular collapse. Monocyte chemoattractant protein-1 (MCP-1), a cytokine that activates endothelial repair in response to injury (*28*), increased approximately sixfold relative to the immediate postdose serum levels in a time course roughly inverse to platelet count decrease. Plasma serotonin did not change through 90 min but was increased immediately before euthanasia, which does not support a role for platelet-induced release of serotonin in the mechanism of toxicity.

These data indicated that A-1331852 was causing apoptosis selectively in the capillary endothelial cells within the heart, leading to structural damage and edema within interstitial heart tissue and in the cardiomyocytes. To further investigate whether the observed cardiovascular toxicity was on-mechanism, we evaluated several tool molecules (Fig. 1E) in anesthetized dogs following the same study design (fig. S1). The analog 2 caused the same constellation of effects as A-1331852, although the effects took slightly longer to manifest (90 to 115 min), possibly resulting from lower potency and slightly decreased plasma exposure. In contrast, the structurally related but functionally inactive molecule 3 (Fig. 1E) did not induce thrombocytopenia, nor did it affect any other measured parameters. These results provided compelling evidence that the observed cardiovascular effects were mechanism-driven. As we recently reported, combining structural elements of both the A-1331852 and navitoclax pharmacophores afforded the potent and selective molecule 4 that is distinct in structure as assessed by an objective cheminformatic evaluation, thus rendering an additional tool for investigating structural versus target-based effects (*29*). Bolus infusion of 4 into anesthetized dogs afforded a lower exposure than A-1331852 (Fig. 1F); despite this difference and the lower potency of this molecule, the signature toxicity was observed in one of two dogs at 175 min. These data further supported that BCL-X_L inhibition was driving severe cardiovascular damage. These results prompted the assessment of the dual BCL-X_L/BCL-2 inhibitor

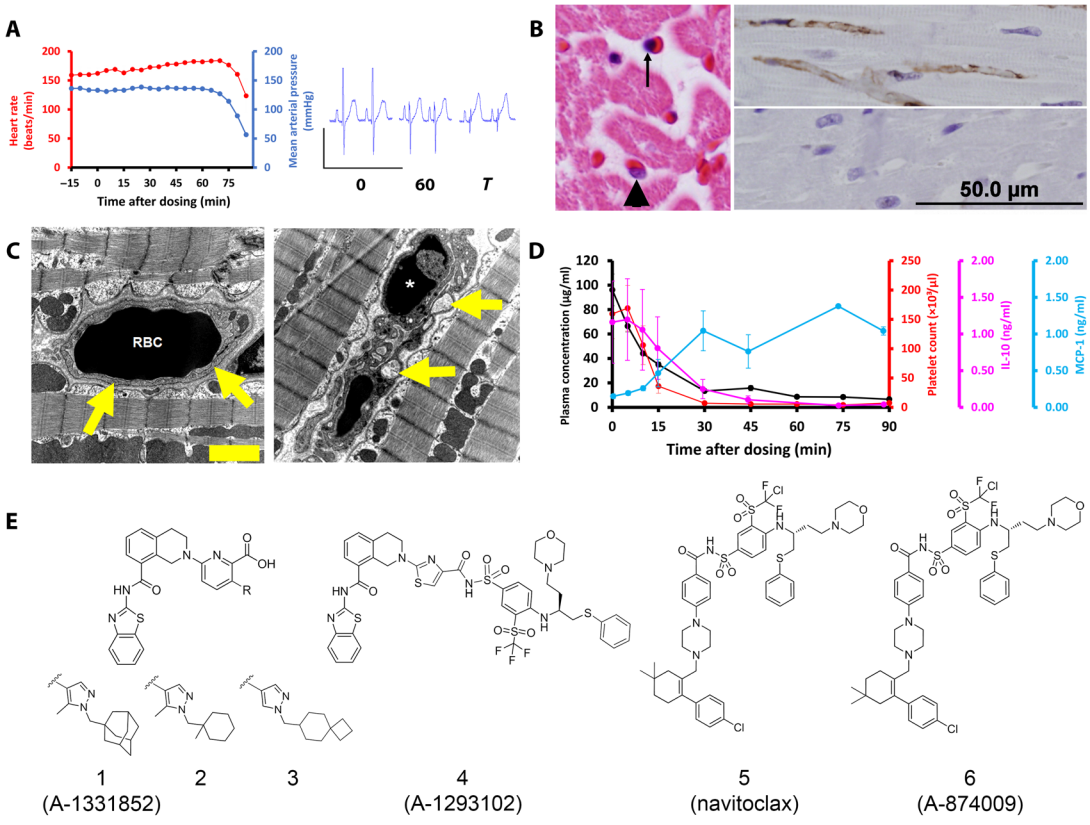

F

Entry	Molt-4 cell EC_{50} (nM)[a]	RS4;11 cell EC_{50} (nM)[a]	Dog $C_{5\ min}$	Dog $C_{90\ min}$
1 (A-1331852)	6.3	>5000	66.5	6.6[b]
2	94	>5000	41.4	10.5
3	>5000	>5000	82.7	24.9
4 (A-1293102)	80	>5000	8.6	0.061
5 (Navitoclax)	303	112	NT	NT
6 (A-874009)	134	28	18	12.2

[a] 48 hours, 10% human serum (HS). [b] Terminal plasma samples were taken at study termination (<90 min).

Fig. 1. BCL-X_L–selective inhibitors cause on-target cardiovascular toxicity in dogs. (**A**) In instrumented, anesthetized beagle dogs' heart rate and mean arterial blood pressure drop precipitously approximately 60 min following an intravenous bolus dose (2.5 mg/kg) of A-1331852 (left; $n = 2$). Marked reduction in R-wave amplitude in electrocardiogram tracings at 0 and 60 min after dosing (right). (**B**) Left: Hematoxylin and eosin–stained heart demonstrates nuclear pyknosis of an endothelial cell (arrow) and a comparatively normal nucleus (arrowhead). Top right: Cardiac endothelial cells are immunoreactive (brown) for activated caspase-3 in an A-1331852 (2.5 mg/kg)–treated dog 90 min after dosing, whereas no activated caspase-3 is detected in a dog treated with structurally related inactive compound 3 (2.5 mg/kg) that does not cause cardiovascular collapse (bottom right). (**C**) Electron photomicrograph of a myocardial capillary from dog treated intravenously with active compound 2 (left), approximately 90 min after an intravenous dose (2.5 mg/kg). An erythrocyte [red blood cell (RBC)] is present within a well-defined capillary (arrows). Right: The endothelium is collapsed with condensed nuclear material (*) and intracytoplasmic vesicles (arrows) approximately 90 min following an intravenous dose (2.5 mg/kg) of a potent SMI 2. Scale bar, 2 μm (on electron micrograph). (**D**) Plasma A-1331852 is rapidly cleared following an intravenous dose (2.5 mg/kg), shown as mean from the same two dogs. Platelet count and serum IL-10 rapidly fall from baseline levels following dosing, whereas serum MCP-1 increases and remains elevated from 30 min after dosing. Error bars are SEM. (**E** and **F**) Structure, binding affinity, and cellular potency of molecules used in anesthetized dog studies and navitoclax, as well as the plasma concentration (in micrograms per milliliter) of each molecule evaluated in the dog studies at 5 and 90 min after initiation of study. The RS4;11 and Molt-4 cell lines are dependent on BCL-2 and BCL-X_L, respectively. NT, not tested.

A-874009 (6) (*16*), a close structural analog of navitoclax. Bolus infusion of A-874009 imparted severe thrombocytopenia in both dogs and moderate caspase activation in the heart of one of two dogs (fig. S2, A and B) yet notably caused minimal impact on cardiovascular function. These data suggested that selective BCL-X_L SMIs, but not the dual BCL-X_L/BCL-2 SMIs, were highly cardiotoxic in dogs at the doses and concentrations evaluated. This may be partially explained by the lower potency of the dual inhibitors in combination with decreased heart exposure after infusion. In addition, the possibility of the dual inhibitor local concentration in the capillary endothelium being effectively reduced via BCL-2 binding cannot be ruled out.

A subsequent study was performed in which two anesthetized cynomolgus monkeys were administered either a bolus (2.5 or 5 mg/kg) of A-1331852 and toxicokinetic and observational end points were recorded. Evidence of apoptosis in the heart was observed, although to a lesser extent than in dog, with one mortality in the group (5 mg/kg; fig. S3). In contrast, no signs of severe cardiovascular injury were observed in anesthetized rats up to very high plasma concentrations (table S2), with only a moderate decrease in MAP observed during the last infusion period. These data indicated a difference in physiology and cardiovascular sensitivity to BCL-X_L inhibition across species with the higher species, particularly dogs, being more sensitive than rodents. Furthermore, the impact on the cardiovascular system was not a monitorable response and, upon initiation of the decrease in MAP and other parameters, did not appear to have any signs of reversibility. As there was seemingly no means of establishing safety in humans, the selective BCL-X_L SMI drug discovery program was terminated.

BCL-X_L–targeting ADC AM1-15 inhibits tumor growth and spares platelets in mice

Considering these results and its established role in tumor maintenance, we conducted research to investigate whether BCL-X_L could be targeted safely via an ADC approach. To first effect the transformation of the large and hydrophobic SMIs to viable ADC payloads, we undertook experiments to determine whether the introduction of charged polar moieties into the pharmacophore could increase the solubility of the drug-linker and confer suitable drug-like properties to the corresponding ADCs. We also proposed that charged groups on the payload could limit cellular permeability; in the event that any free payload was liberated from the conjugate, lower permeability could provide an additional mitigation against toxicity resulting from systemic BCL-X_L inhibition.

X-ray structural observations were used to design a pair of linkable BCL-X_L–targeting warhead with differentiated physicochemical properties and cellular permeability. We started by generating the x-ray cocrystal structure of literature compound A-1331852 (Fig. 2A) bound to BCL-X_L protein. The elasticity of the hydrophobic P4 pocket indicated that potency gains could be realized via additional hydrophobic substitution on the adamantane. In addition, the protein-bound pose of A-1331852 revealed a solvent-exposed exit vector from the adamantane as a potentially suitable site for installation of an amine-based linker attachment and structural modifications that could modulate molecule permeability and solubility (Fig. 2B). The first concept led to the generation and evaluation of 3,5-dimethyladamantane analog 8, which gratifyingly demonstrated nearly 10-fold improvement in cell killing in the BCL-X_L–dependent Molt-4 cell line (*16*) relative to compound 7 (Fig. 2B). Substitution of the methyl ether of 8 with ethoxyamino-methyl and ethoxyamino-ethylsulfonic acid units rendered linkable BCL-X_L–targeting warheads 9 and 10, respectively.

Compounds 9 and 10 retained the target binding affinity of analog 8, supporting a solvent-exposed and noninterfering vector of the ethoxyamino linking units (Fig. 2B). While compound 9 demonstrated a median effective concentration (EC_{50}) of 8 nM in the Molt-4 cell viability assay, the sulfonic acid 10 lost over 30-fold activity, suggesting a permeability difference between the molecules. As commonly used permeability assays rendered no usable data for this compound class (*24*), we performed an assessment of mitochondrial depolarization in Molt-4 cells permeabilized with digitonin (*30*), which creates pores within the outer cell membrane, thus temporarily alleviating the need for the permeabilization process. In the setting of relaxed permeability constraints, both 9 and 10 elicited subnanomolar EC_{50} values. Together, these data supported divergent permeability as the driver of the cellular activity differences between the two compounds.

A single dose of compound 9 or 10 was then administered to mice to evaluate the impact of compound properties on platelets in vivo. While a low dose of 0.1 mg/kg was selected for the more permeable 9, a higher dose (0.6 mg/kg) of 10 was chosen to match the molar equivalent of payload contained within a dose (30 mg/kg) of an ADC containing an average drug-antibody ratio (DAR) of 4 (*19*). Inhibitor 9 induced severe thrombocytopenia ($P < 0.001$) by 6 hours that was similar to navitoclax at 50 mg/kg ($P < 0.001$). Notably, no significant reduction of platelet number was observed in mice treated with 10 ($P = 0.51$; Fig. 2D). This prompted the evaluation of the two compounds for cardiovascular safety in anesthetized dogs using the same study design as described earlier. Along with the expected thrombocytopenia, 9 caused marked changes in cardiovascular parameters at low dose (0.03 mg/kg) and plasma concentration ($C_{5\ min} = 0.091$ μg/ml), which included a decrease in MAP and a reduction of the QRS amplitude (Fig. 2E and table S3). In contrast, bolus infusion of 10 caused only minimal to moderate effects on cardiovascular parameters and no decrease in platelets (Fig. 2F and table S4), despite much higher dose (2.5 mg/kg) and concentration ($C_{5\ min} = 9.24$ μg/ml). These data confirmed that systemic effects of released SMI could be mitigated by modulation of the payload permeability.

To next assess the ability of compounds 9 and 10 to function in the context of an ADC, we coupled each individually to the clinically validated and protease-labile maleimidocaproyl valine citrulline *p*-aminobenzyloxycarbonyl (MCVC-PABC) linker 13 (*31*) to afford drug-linkers 14 and 15 (Fig. 3A). For the antibody component, a bioinformatics analysis using the Human Protein Atlas (proteinatlas.org) and internal tissue banks indicated that EGFR fulfilled the prespecified antigen criteria of high tumor but limited heart or platelet expression. The well-behaved anti-EGFR antibody AB033 (*32*), a close analog of the clinically validated antibody cetuximab (*33*), was selected as an initial tool and conjugated to 14 and 15 to render the fully constructed ADCs AB033-14 and AB033-15, respectively (Fig. 3A). AB033-14 showed very high levels of aggregation in buffer, thus reflecting physical properties incompatible with further development (Fig. 3B). In contrast, the soluble drug-linker–containing ADC AB033-15 showed low levels of aggregation [<3% high molecular weight species (HMWS)] in buffer (Fig. 3C) that were equivalent to the marketed auristatin-based brentuximab vedotin (*31*) in a head-head assessment (table S5).

To investigate the ability of AB033-15 to inhibit cell growth in an antigen-dependent and BCL-X_L–mediated fashion, we transfected *mcl1*$^{-/-}$ mouse embryonic fibroblast (MEF) cells, which have been reported to be dependent on BCL-X_L for survival (*34*), with a retroviral construct containing the human EGFR sequence or an empty vector control to afford an isogenic pair of cell lines. AB033-15 inhibited growth of the human EGFR–expressing (huEGFR$^+$) *mcl1*$^{-/-}$ MEF cells with an EC_{50} of 0.035 nM yet showed >10,000-fold lower growth inhibition of the isogenic *mcl1*$^{-/-}$ MEF cells lacking human EGFR ($EC_{50} = 506$ nM). Administration of an ADC containing drug-linker 15 conjugated to an anticytomegalovirus antibody (*35*) (MSL109-15) demonstrated much lower activity ($EC_{50} = 845$ nM) in the huEGFR$^+$

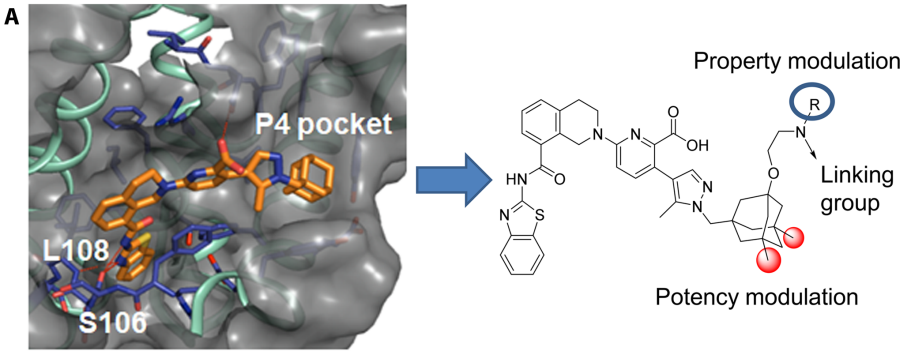

B

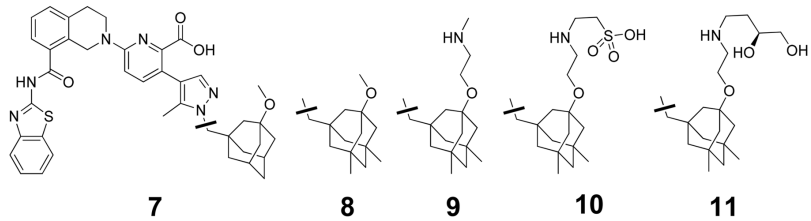

Entry	BCL-X_L TR-FRET K_i (nM)	Molt-4 cell EC_{50} (nM)[a]	Permeabilized Molt-4 EC_{50} (nM)[b]
7	<0.01	8.4	NT
8	<0.01	0.9	NT
9	<0.01	7.7	0.42
10	<0.01	259	0.15
11	<0.01	77.8	0.07

[a] 48 hours, 10% human serum. [b] 1 hour, no human serum.

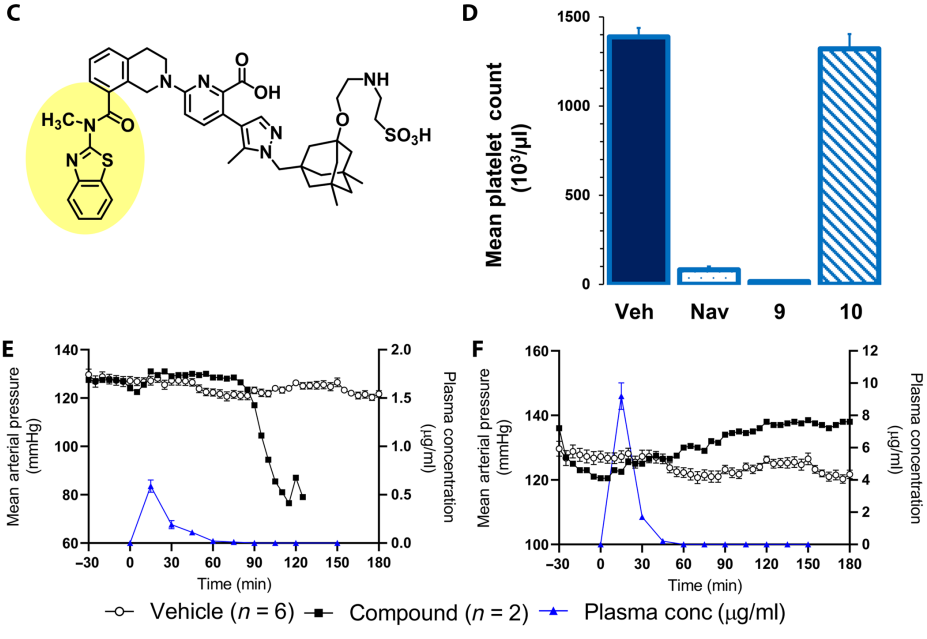

Fig. 2. Discovery of linkable BCL-X_L inhibitors with different solubility and permeability properties affords putative ADC payload component with high target affinity yet minimal systemic toxicity in mice and dogs. (**A**) X-ray cocrystal structure of BCL-X_L bound to A-1331852 (1.93 Å; Protein Data Bank code 9AQZ; see the Supplementary Materials) and key regions of the BCL-X_L inhibitor pharmacophore for modification as derived from the x-ray structure. (**B**) Binding, cellular potency in Molt-4 cells, and functional potency in digitonin-permeabilized Molt-4 cells of BCL-X_L inhibitors. (**C**) Structurally related inactive inhibitor 11; methylation of P2-binding amide bond nitrogen disrupts key hydrogen binding network and leads to full ablation of cellular activity. (**D**) Platelet count 6 hours after treatment with BCL-X_L inhibitors in heparinized whole mouse blood. Navitoclax (50 mg/kg) was given orally, and 9 (0.2 mg/kg) and 10 (0.6 mg/kg) were intravenously administered. Each bar represents the average platelet count in five SCID/bg mice. Error bars depict the SEM. (**E** and **F**) MAP of dogs administered vehicle (black filled circles) or BCL-X_L inhibitor (open circles) and plasma concentration of BCL-X_L inhibitors (blue triangles) following an intravenous bolus dose of either 9 or 10.

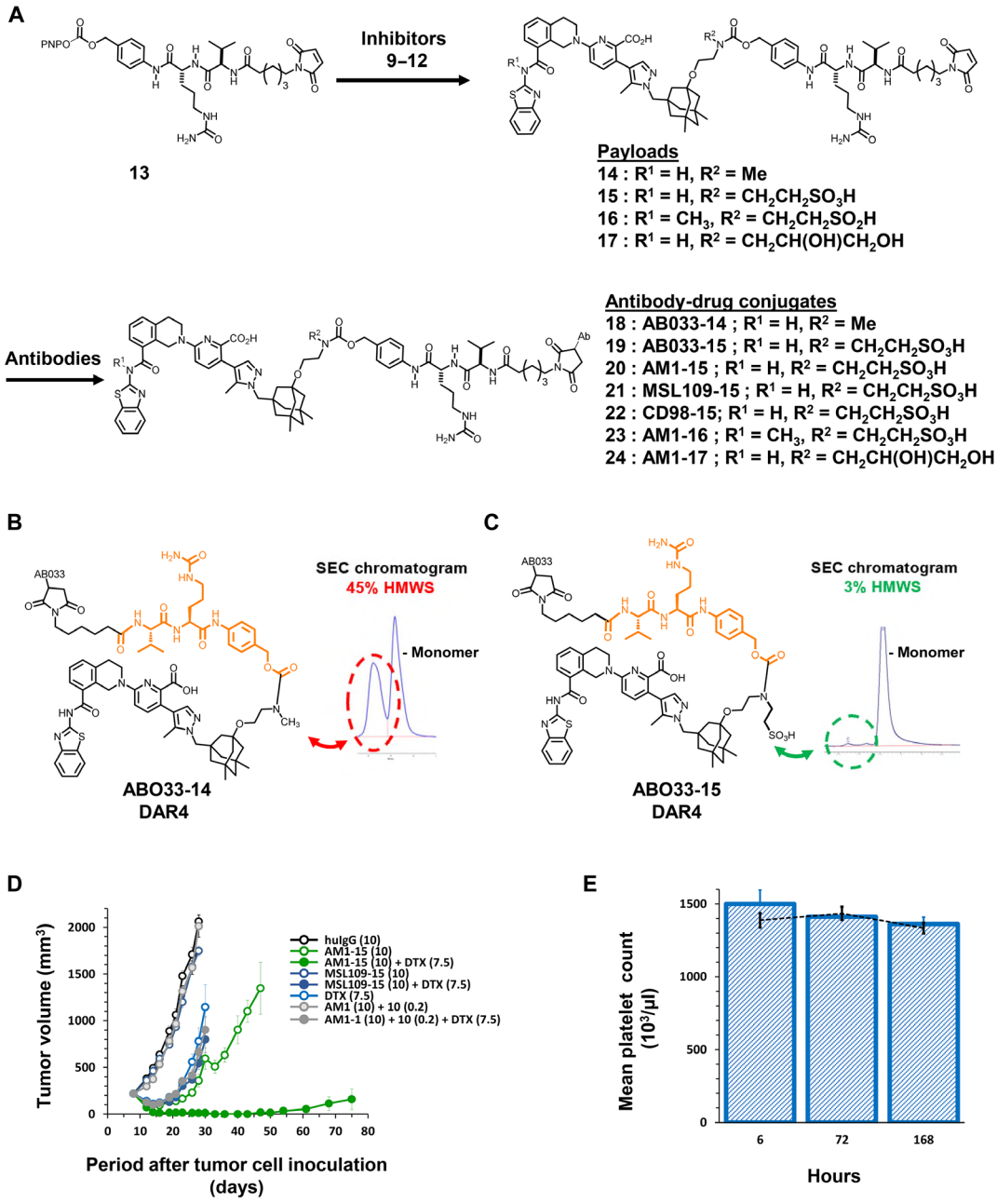

Fig. 3. Modification of payload leads to ADC (AM1-15) with robust in vivo efficacy and no thrombocytopenia in mice. (**A**) General synthetic scheme for coupling inhibitors 9 to 12 to linker 13 to afford drug-linkers 14 to 17 and subsequent conjugation of drug-linkers 14 to 17 with antibodies targeting EGFR (AB033 and AM1), CD98 or a nontargeted control (MSL109) immunoglobulin G1 (IgG1) antibody to generate ADCs 18 to 24. (**B** and **C**) Aggregation profiles of ADCs AB033-14 and AB033-15 in pH 7.4 buffer as assessed by size exclusion chromatography (SEC) and presence of HMWS. (**D**) The volume of subcutaneous H1650 tumors was plotted as a function of the time after tumor inoculation. SCID/bg mice with a subcutaneous tumor of approximately 200 mm^3 were treated with AM1-15 or MSL109-15 at dose levels of 10 mg/kg. The conjugates were given as either single agent (open symbol) or in combination with docetaxel (DTX) (closed symbol). Treatment started at day 9 after tumor inoculation. An unconjugated mixture of AM1 and free inhibitor 10 was administered with (closed symbol) or without docetaxel (open symbol). Conjugates, antibody, and inhibitor 10 were intraperitoneally administered at a QDx1 (every day for one dose) regimen. Docetaxel was administered intravenously at 7.5 mg/kg (QDx1). Dose levels of each treatment (in milligrams per kilogram) are specified between brackets in the legend. Each point of a curve represents the arithmetic mean of the volumes of eight tumors. Error bars depict the SEM. (**E**) Platelet count after treatment with AM1-15 (bars) compared to treatment with vehicle (dashed line) in heparinized whole mouse blood. AM1-15 was administered intravenously at 30 mg/kg. Each bar and data point represent the average platelet count in five mice. Error bars depict the SEM.

MEF cells and little differentiation in activity between the isogenic pairs ($mcl1^{-/-}$ MEF EC_{50} = 446 nM). These data provided evidence that AB033-15 was exerting on-target and antigen-dependent activity in a BCL-X_L–dependent cell line (fig. S4).

The encouraging results with AB033-15 led to the assessment of drug-linker 15 conjugated to antibody AM1 (*36*), an affinity-matured variant of the humanized EGFR antibody depatuximab (depatux, ABT-806) that binds selectively to the EGFR VIII mutant and a cryptic epitope revealed by EGFR overexpression. The selectivity of AM1 for VIII and overexpressed EGFR over wild-type EGFR offered the potential for selectively targeting tumor tissue and thus alleviating the typical cetuximab-associated side effects associated with normal tissue targeting (*33*). The resultant AM1-15 showed similarly favorable aggregation properties and was highly soluble in histidine buffer (pH 6; 45 mg/ml) at 4°C, revealing the remarkable ability of the ionizable sulfonic acid group of 10 to impart robust solubility properties to an ADC. Additional physical characterization of AM1-15 revealed good stability and minimal (<0.05%) payload release upon incubation in human serum (table S6). In huEGFR$^+$ $mcl1^{-/-}$ MEF cells, AM1-15 demonstrated a nanomolar EC_{50} (54.0 nM) and notably lower activity in the isogenic $mcl1^{-/-}$ MEF cells (EC_{50} = 721 nM). The lower activity in the huEGFR$^+$ $mcl1^{-/-}$ MEF cells is at least a partial reflection of the substantially lower affinity of AM1 for EGFR relative to AB033 (fig. S4) (*36*).

Previous reports have indicated that, while BCL-X_L SMIs show mild in vitro activity in cell lines derived from non–small cell lung cancer (NSCLC) and other solid tumors, synergistic cell killing occurs upon addition of taxane-based agents (*16*). These data reflect a dual dependency of these tumors for both BCL-X_L and MCL-1. Microtubule-targeting agents such as taxanes induce a mitotic arrest, during which MCL1 protein levels decline via a posttranslational mechanism (*37*). The decrease in prosurvival MCL-1 places a greater burden on BCL-X_L for survival and hence greater sensitivity to BCL-X_L inhibitors. Similar to SMIs, ADCs AB033-15 and AM1-15 demonstrated limited single-agent activity in the EGFR-expressing lung adenocarcinoma cell line NCI-H1650 (H1650). However, titration of increasing concentrations of docetaxel markedly sensitized the tumor cells to AB033-15 and AM1-15 (fig. S5).

To assess this combinatorial antitumor activity in vivo, we treated immunocompromised mice bearing H1650 tumors with AM1-15 at a single dose of 10 mg/kg, docetaxel, or the combination of both. As controls, separate groups of mice were dosed with the molar equivalent of free inhibitor 10 in combination with the unconjugated AM1 antibody, the nontargeting ADC control MSL109-15 or the combination of MSL109-15 with docetaxel. No signs of distress or weight loss were apparent in any animal group. Although all treatments resulted in a statistically significant ($P < 0.01$) tumor growth inhibition (TGI), the treatment with MSL109-15 or the combination of AM1 and 10 induced only marginal (<60%) inhibition of 19 or 24%, respectively. Addition of AM1 plus 10 or MSL109-15 to docetaxel failed to significantly increase ($P > 0.07$) the efficacy of docetaxel monotherapy. In contrast, combination treatment of AM1-15 with docetaxel inhibited tumor growth by 100%. This inhibition was significantly ($P < 0.01$) higher than that caused by AM1-15 (89%) or docetaxel (81%) alone. The increase in efficacy of the combination therapy was also reflected in significantly increased durability ($P < 0.01$) as compared to docetaxel or AM1-15 administered as single agent. Following combination treatment, only two of eight tumors relapsed to a tumor volume of 1000 mm^3 within an observation period of 100 days. All tumors were relapsed in the AM1-15 and docetaxel groups within 46 days after treatment (Fig. 3D). In total, these results demonstrated that AM1-15 caused antitumor activity, both as monotherapy and in combination with docetaxel, which was dependent on antigen-specific delivery.

In a separate experiment, we measured platelet levels in mice following a single and higher (30 mg/kg) dose of AM1-15 and observed no thrombocytopenia through 14 days (Fig. 3E), indicating that neither the ADC nor any liberated inhibitor was significantly ($P > 0.35$) reducing the number of mature platelets. Together, these data supported the concept that an ADC approach could have antitumor efficacy while mitigating the systemic toxicity imparted by BCL-X_L SMIs.

AM1-15 is well tolerated in monkeys yet causes unprecedented kidney effects

Encouraged by the in vivo proof-of-concept studies in mice, we next evaluated the tolerability of AM1-15 in cynomolgus monkeys. A single-dose escalation study was first conducted with AM1-15 (DAR4) at dose levels ranging from 3 to 30 mg/kg. AM1-15 was well tolerated at all doses with no clinical signs of cardiovascular distress, and the exposure increases [total antibody (TAb)] were dose proportional (table S7). On the basis of these results, a dose-range finding toxicology study was performed where monkeys were administered AM1-15 (0, 10, or 30 mg/kg) every week for three doses (Q1W×3) or 30 mg/kg Q3W×2, followed by a necropsy 1 week after the last dose. AM1-15 displayed near dose-linear exposure with respect to TAb, with mean half-lives ranging 3 to 7 days (tables S8 and S9). Maximum free concentration of 10 occurred between 4 and 32 hours and escalated in near dose-linear fashion across the same dose range (mean C_{max} at 30 mg/kg = 20 ng/ml for 24 hours). No clinical or histopathologic evidence of cardiovascular toxicity was observed; however, other cardiovascular parameters were not evaluated.

A dose-dependent thrombocytopenia (up to 64% decrease in platelets from individual baseline at the 30 mg/kg Q3W×2 and nadir of 110,000 platelets/μl) and anemia [up to 33% decrease in red blood cell (RBC) mass from individual baseline at the dose of 30 mg/kg] were observed in monkeys. As platelets were not monitored in the previous cardiovascular study with A-1331852 in monkeys, no direct comparison could be made. However, a near complete clearance of circulating platelets following a single dose of A-1331852, navitoclax, and other SMIs in mice and dogs occurred at doses at or lower than those demonstrating in vivo efficacy. In contrast, the thrombocytopenia caused by AM1-15 at 30 mg/kg would not be considered dose limiting, given the absolute nadir (clinical grade 3 thrombocytopenia 25,000 to 50,000 platelets/μl), nor would the levels be considered a risk for spontaneous bleeding (<10,000 platelets/μl) (*38*). In total, these data supported a substantially improved TI with respect to this hematological parameter for AM1-15 relative to the SMIs.

While the ADC was tolerated overall, histopathology from repeat dose studies uncovered a dose-dependent effect in the kidney characterized by a diffuse increase in glomerular matrix (Fig. 4, A and B), along with occasional degenerate cells and mitotic figures in the renal glomeruli (Fig. 4, C and D). This effect was observed in all glomeruli and in all monkeys dosed with AM1-15 regardless of dosing regimen. The histologic nature of this finding was suggestive of an immune mediated glomerulopathy occasionally seen following administration of humanized biologics to preclinical species (*39*, *40*). However, there was neither a drop in TAb exposure nor formation of antidrug antibodies that

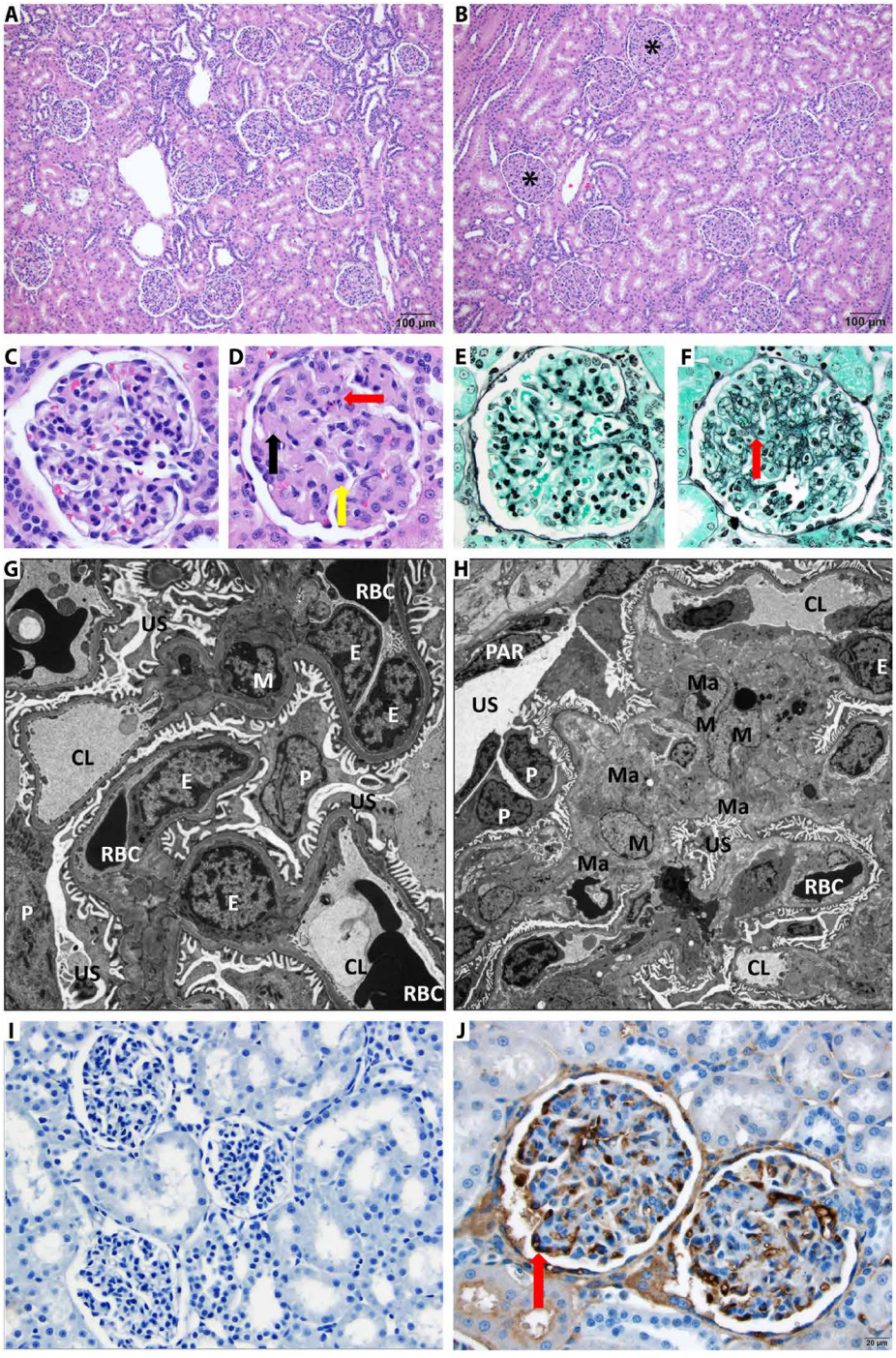

Fig. 4. Multiple dose administration of AM1-15 to cynomolgus monkeys causes unique renal toxicity. Hematoxylin and eosin–stained kidney from control (**A**) and treated cynomolgus monkey (**B**). There is diffuse thickening of glomerular matrix in the AM1-15–treated kidney (asterisk). Scale bar, 100 µm. At high magnification as compared to control monkey glomeruli (**C**), the AM1-15–treated glomeruli (**D**) has global thickening of glomerular matrix by eosinophilic material (black arrow), and occasional degenerate cells (red arrow) and mitotic figures (yellow arrow) are also present. Periodic acid methenamine stain revealed an increased mesangial matrix component (red arrow) in the AM1-15–treated glomeruli (**F**) as compared to control monkey glomeruli (**E**). Electron microscopy revealed enlarged mesangial cell with increased cytoplasm (hypertrophy) along with moderate increase in extracellular mesangial matrix deposition in the AM1-15–treated glomeruli (**H**). The rest of the glomerular components, namely, endothelial cells, podocytes, and filtration apparatus, was within normal limit as compared to control glomeruli (**G**). M, mesangial cell; Ma, mesangial matrix; E, endothelial cells; P, podocyte; PAR, parietal epithelium; US, urinary space; CL, capillary space; RBC, red blood cell. Magnification, ×6000 (G) and ×3000 (H). (**I** and **J**) Anti–BCL-X_L drug-linker–specific monoclonal antibody was synthesized, and IHC was performed to visualize the distribution of drug-linker. Moderate-to-strong immunoreactivity was observed in glomerular endothelial cells (red arrow) in a cynomolgus monkey administered AM1-15 (J) (scale bar, 20 µm) as compared to control (I).

would support an immune complex disease. To further characterize the nature of renal toxicity, we conducted special stains (periodic acid–Schiff stain and periodic acid methenamine stain) and electron microscopy.

Special stains revealed an increase in deposition of mesangial matrix (Fig. 4, E and F), which was essentially uniform in all glomeruli bilaterally. Electron microscopy revealed enlarged mesangial cells with increased cytoplasm (hypertrophy) containing prominent rough endoplasmic reticulum along with a moderate increase in mesangial matrix deposition (Fig. 4, G and H), thus supporting the special stain results. No antigen-antibody complexes were noted, excluding the possibility that the humanized antibody was driving immune complex formation in the monkey kidneys. In addition, minimal impact was observed in podocytes and capillary endothelial cells, indicating a highly selective effect on mesangial cells within the glomeruli.

To our knowledge, this effect has not been reported with any previous biologic agents or small molecules against any biological target. The AM1-15-induced expansion of mesangium in the absence of demonstrable immune complexes suggested a distinct mechanism for the accumulation of AM1-15 in the glomerulus. We hypothesized that the plasma aggregation of the broad DAR4 AM1-15, which increases over time, may have led to aggregate deposition within the kidney and subsequent stimulation and hypertrophy of the mesangial cells. AM1-15 was thus purified to DAR2 by hydrophobic interaction chromatography (HIC), which resulted in lower initial aggregation in plasma (table S10). The DAR2 construct was then evaluated in a 4-week monkey study, where the pharmacokinetic data showed similar profiles of TAb and conjugated ADC between DAR4 and DAR2 at a dosing of 30 mg/kg weekly, while the DAR2 resulted with the lower conjugated payload concentrations in circulation (Fig. 5A). However, in this monkey study, repeat dosing of AM1-15 (DAR2) still caused the signature kidney lesion. These data refuted the postulate that high initial plasma aggregation was a key contributor to the observed renal toxicity.

A series of toxicology studies were conducted to explore the role of antigen and payload in the observed renal toxicity (tables S11 and S12). These included the administration of ADCs containing antibodies targeting either a nontargeting (MSL109-15) or distinct antigen (CD98-15; Fig. 3A) (*41*) to monkeys at 10 mg/kg once a week for 3 weeks. Last, an ADC (23; Fig. 3A) containing AM1 conjugated to the structurally related yet functionally inactive payload 16 (AM1-16; Fig. 2C) was included. Regardless of the antibody used, all ADCs containing an active payload showed similar effects within the kidney (see tables S8 and S9 for toxicokinetic data). In contrast, the functionally inert AM1-16 showed no renal effects. These data provided intriguing evidence that the observed mesangial cell hypertrophy was driven by inhibition of BCL-X_L in the kidney. To investigate the possibility that payload was accumulating in the kidney tissue, we generated an anti–BCL-X_L drug-linker IHC reagent and stained kidney tissue from monkeys that have been treated with AM1-15. Moderate-to-strong staining was observed, providing evidence that drug-linker 15 was present within glomerular endothelial cells (Fig. 4, I and J) following repeat dosing.

Modification of drug-linker affords ADC with vivo efficacy and favorable properties

The aforementioned studies provided evidence that free nonpermeable inhibitor 10 was accumulating in the kidneys and that resultant BCL-X_L inhibition was driving the mesangial cell hypertrophy within the glomeruli. We then investigated whether the kidney lesion may be alleviated by increasing the permeability of the inhibitor, thus allowing it to escape the tissue and relieve the constitutive inhibition of BCL-X_L. However, the observation that more permeable molecules such as A-1331852 cause severe thrombocytopenia and cardiovascular toxicity in nonrodent mammalian species clearly indicated that a delicate balance of permeability between compounds 9 and 10 would be critical. To this end, we investigated whether incorporation of appropriate hydrogen bond donors (*42*) into the solvent-exposed appendage of 9 could yield linkable warheads capable of achieving the desired property balance. A series of molecules containing solvent-exposed polyol units was then generated. The diol 11 (Fig. 2B) was particularly compelling given its high binding affinity and intrinsic potency in permeabilized Molt-4 cells, yet activity in nonpermeabilized Molt-4 cells that was intermediate with respect to 9 and 10.

Coupling of 11 to precedented linker 13 afforded a drug-linker (17; Fig. 3A) with solubility (Sol7.4 < 0.0011 mg/ml) insufficient for further antibody coupling; this result indicated that a linker with enhanced solubilization properties would be required to enable the incorporation of 11 into drug-like ADCs. In assessing the components of the well-behaved drug-linker 15 (Fig. 3A), we thus considered for modification three substructural units of the linker region: the PABC spacer, the dipeptide cleavable unit, and the antibody attachment group. Extensive investigation into modified PABC moieties led to the incorporation of a solubilizing C-linked glucuronide (*23*) in a manner that would minimally disrupt the steric environment of the dipeptide cleavage site (Fig. 5B). Parallel exploration of the latter indicated the valine-alanine dipeptide trigger to be an optimal replacement of the more hydrophobic valine-citrulline congener. Last, to bias the linker terminus toward hydrophilicity and stability, we designed the disubstituted pyrrolidin-2-one moiety with two key features in mind; the highly polar and ionized sulfonic acid to impart solubility and the electronically activated maleimide moiety to enable mild (pH 8) chemical hydrolysis of the intermediate succinimide species obtained immediately after antibody conjugation. It was envisioned that this hydrolysis to afford the linear 4-oxopentanamide terminus would impede spontaneous loss of drug-linker by retro–hetero-Michael addition of the monoclonal antibody sulfide moiety (Fig. 5C). Chemical synthesis and coupling of these components with payload 11 (see Materials and Methods), followed by conjugation to AM1 and purification yielded AM1-25. This ADC exhibited excellent drug-like properties, including low aggregation in buffer and mouse, monkey, and human plasma (<2% HMWS; table S10) and less than 0.14% payload release in cross-species plasma after a 5-day incubation.

The in vivo efficacy of AM1-25 was next evaluated alongside AM1-15 in immunocompromised mice implanted with H1650 or PC-9 NSCLC tumor cells. Both ADCs were dosed as monotherapy at 10 mg/kg once weekly for 2 weeks or in combination with a single dose of docetaxel. Treatment with AM1, AM1-15, AM1-25, docetaxel, and the combination of docetaxel with AM1-15 or AM1-25 caused statistically significant ($P < 0.01$) TGI of H1650 and PC-9 xenografts as compared to control treatment (Fig. 6, A and B). In the PC-9 model, the combination of AM1-15 or AM1-25 enhanced TGI of docetaxel from 82 to 98 ($P = 0.001$) or 96% ($P = 0.001$), respectively. In the H1650 model, TGI of docetaxel was enhanced from 83 to 99% ($P < 0.0001$) by combining with either conjugate. In

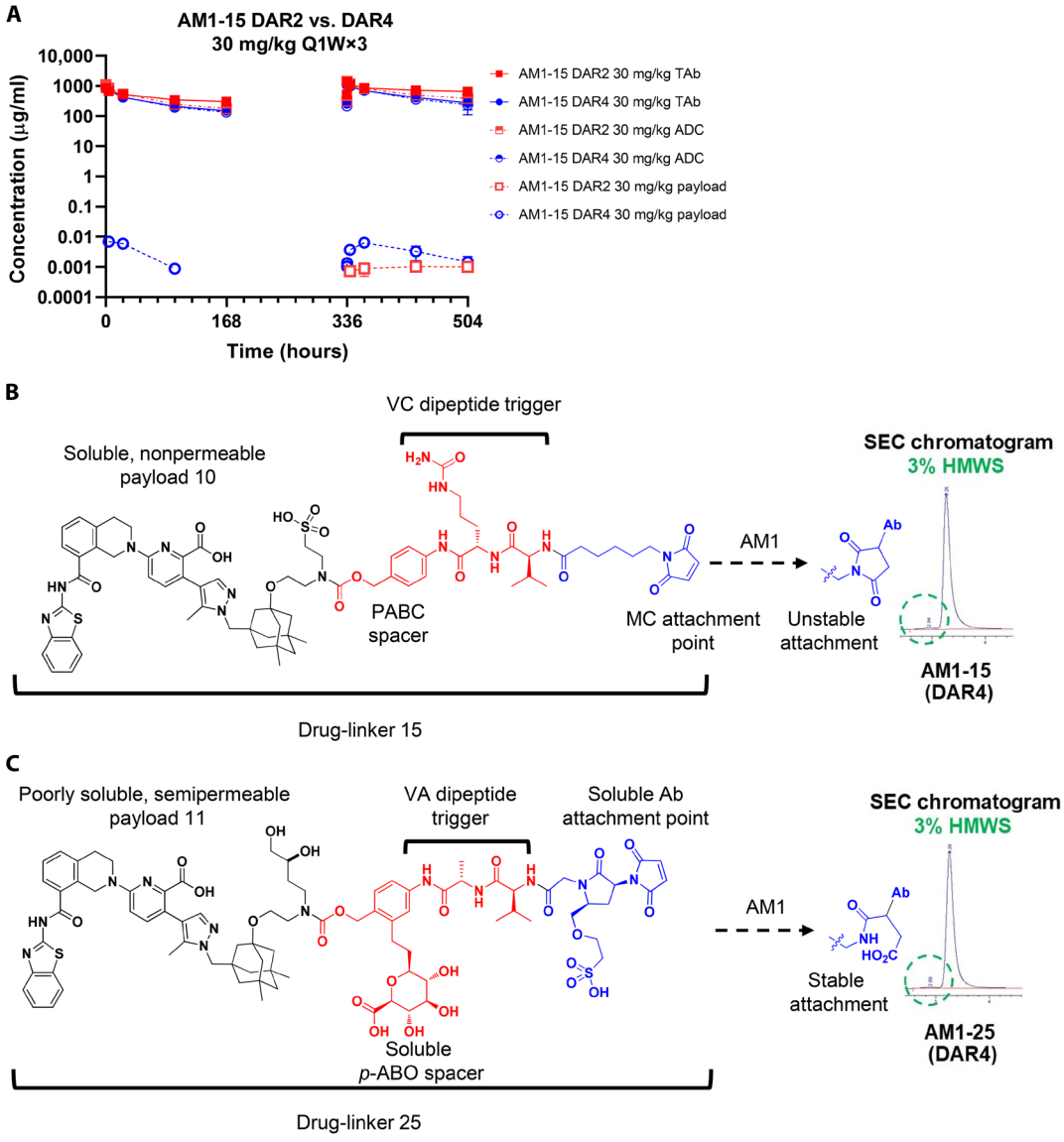

Fig. 5. Monkey pharmacokinetics of AM1-15 DAR4 and purified DAR2 and modification of drug-linker for solubility enable the utility of semipermeable inhibitor 11 in the context of drug-like ADC AM1-25. (**A**) AM1-15 (broad DAR4) and AM1-15 DAR2 show linear pharmacokinetics in monkeys, and DAR purification to 2 reduces free payload in circulation. (**B**) Components of intact drug-linker 15 and aggregation profile of corresponding DAR4 AM1-15 ADC in pH 7.4 buffer as determined by SEC. VC, valine-citrulline; MC, maleimidocaproyl. (**C**) Components of enabling drug-linker 25 including solubilized *para*-aminobenzyloxy (*p*-ABO) spacer, valine-alanine (VA) dipeptide trigger unit and solubilized antibody attachment unit, and aggregation profile of corresponding DAR4 AM1-15 ADC in pH 7.4 buffer as determined by SEC.

both models, the increase in efficacy of the combination therapy was also reflected in significantly increased durability ($P < 0.01$) of the response to docetaxel combined with AM1-15 or AM1-25 as compared to docetaxel given as single agent.

These encouraging data prompted an exploratory study where monkeys were administered the construct of 0, 10, or 30 mg/kg Q3W×2 or 10 mg/kg Q1W×3, followed by a necropsy 1 week after the last dose. A clear reduction in severity of both renal and hematological toxicities was observed. Specifically, the increased glomerular matrix was seen at all dose levels but with reduced penetrance (i.e., multifocal kidney lesions via AM1-25 compared to the diffuse lesions noted with AM1-15). The platelet decrease was minimal even at the highest dose (−19% as compared to individual baseline values) with a nadir of 315,000 platelets/μl and minimal decrease in RBC mass (−5% as compared to individual baseline). The pharmacokinetics of TAb and conjugated antibody increased from 10 to 30 mg/kg in a linear fashion (Fig. 6, C and D, and Table 1). The stability of the drug-linker was reflected by the low plasma concentration of free payload 11 (C_{max} = 1.48 and 4.71 ng/ml at 10 and 30 mg/kg, respectively), following the second dose (day 21). Attempts to evaluate the concentration of the unconjugated payload 11 or attached within drug-linker 25 in kidneys were compromised by technical challenges; these data were collected in later studies and will be disclosed elsewhere.

Last, the plasma concentration of 11 associated with cardiovascular safety in dogs was assessed. Upon infusion of 11 into anesthetized

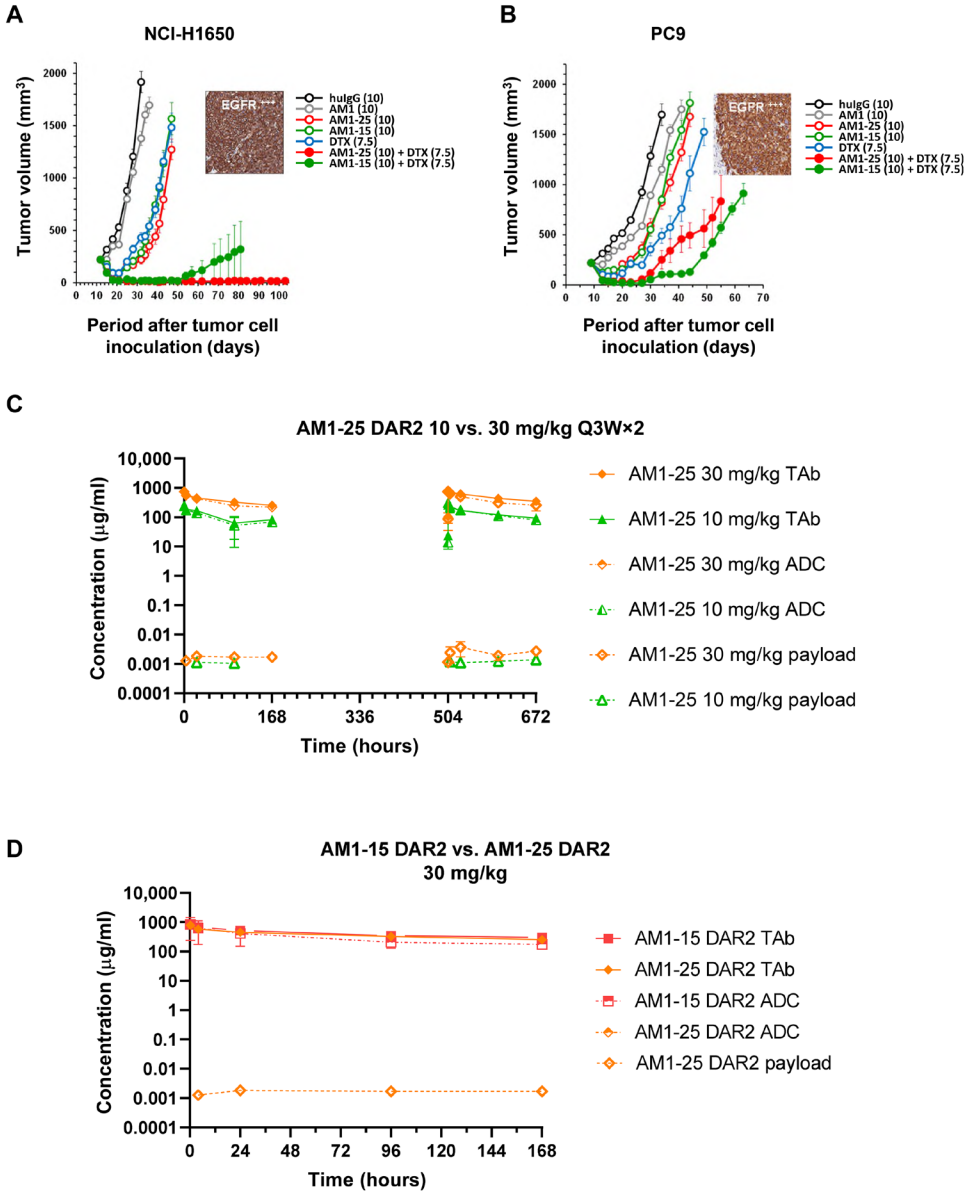

Fig. 6. AM1-25 inhibits tumor growth in vivo and exhibits linear pharmacokinetics in monkeys. (**A** and **B**) The volume of subcutaneous tumors was plotted as a function of the time after tumor inoculation. SCID/bg mice with a subcutaneous tumor of approximately 200 mm^3 were treated with docetaxel, huIgG, AM1, AM1-25, or AM1-15 (open symbols) or a combination of AM1-25 or AM1-15 with docetaxel (closed symbols). The numbers in the legend between parentheses indicates the dose levels (in milligrams per kilogram). Treatment started at day 10 after tumor inoculation. Conjugates and antibody were intraperitoneally administered at a Q7D×2 regimen. Docetaxel was administered intravenously at 7.5 mg/kg (QDx1). Each point of a curve represents the arithmetic mean of the volumes of eight tumors. Error bars depict the SEM. The inset shows EGFR expression of a xenograft as revealed by IHC for H1650 (A) and EBC-1 (B). Concentration-time profiles of TAb, conjugated antibody (ADC), and unconjugated payload following two intravenous doses (10 or 30 mg/kg) of AM1-25 (**C**), or AM1-15 (**D**) 3 weeks apart in cynomolgus monkeys. Data are presented as means ± SD ($N = 3$).

dogs at doses of 0.01 and 0.1 mg/kg per minute, no impact on blood pressure or other indices of cardiovascular function were observed up to a plasma concentration of 447 ng/ml (table S13). A higher dose of 0.3 mg/kg per minute (C_{max} = 1015 ng/ml) produced a notable decrease in MAP, contractility, and cardiac output leading to cardiovascular collapse in both animals (table S14). These data indicated that, as compared to the level of free inhibitor 11 measured at the highest dose in monkeys, the plasma concentration in dogs associated with the highest tolerated dose (0.1 mg/kg per minute) provided an estimated a TI of >65-fold. This level of free warhead was not anticipated to be achievable upon administration of a drug-linker 25-bearing ADC in humans; together with the primary pharmacology and tolerability in monkeys, the demonstrated cardiovascular TI of 11 led to the selection of 25 (from here on, referred to as AAA) as the drug-linker for use in development of BCL-X_L inhibitor ADCs for clinical evaluation.

Table 1. Mean toxicokinetic parameters of total and conjugate antibody and unconjugated payload 11 following two intravenous doses (10 or 30 mg/kg) 3 weeks apart or three weekly doses (10 mg/kg) of AM1-25 in cynomolgus monkeys. C_t, concentration measured at 0.25 hours after dosing; C_{max}, maximal concentration after dosing; C_{trough}, concentration measured before administration of the next dose; NA, not applicable; AUC, area under the curve; *D*, dose. Units for TAb and conjugated antibody: C_t, micrograms per milliliter; C_t/D, (dose-normalized concentration measured at 0.25 hours after dosing; micrograms per milliliter) per (milligram per kilogram); AUC, micrograms-hour per milliliter; AUC/*D*, (micrograms-hour per milliliter) per (milligram per kilogram); C_{trough}, micrograms per milliliter. Units for unconjugated 11 (payload): C_{max}, nanograms per milliliter; C_{max}/D, (nanograms per milliliter) per (milligrams per kilogram); AUC, nanograms-hour per milliliter; AUC/*D*, (nanograms-hour per milliliter) per (milligram per kilogram); T_{max}, hours; C_{trough}, nanograms per milliliter. BQL, below quantitation limit.

	10 mg/kg Q21D			30 mg/kg Q21D			10 mg/kg Q7D		
	Day 1								
	Total	**Conj.**	**Payload**	**Total**	**Conj.**	**Payload**	**Total**	**Conj.**	**Payload**
C_t or C_{max}	245	242	0.750	790	744	1.94	245	362	NA
C_t/D or C_{max}/D	24.5	24.2	0.075	26.3	24.8	0.065	24.5	36.2	NA
$AUC_{0–168h}$	17,835	15,451	61.3	61,874	53,496	279	18,231	22,458	NA
$AUC_{0–168h}/D$	1783	1545	6.13	2062	1783	9.30	1823	2246	NA
T_{max}	NA	NA	24	NA	NA	96	NA	NA	NA
	Day 21						Day 15		
C_{trough}	23.8	13.8	BQL	105	88.2	0.380	123	110	0.427
C_{trough}/D	2.38	1.38		3.49	2.94	0.013	12.3	11.0	0.043
C_t or C_{max}	268	308	1.48	840	741	3.71	368	539	1.82
C_t/D or C_{max}/D	26.8	30.8	0.148	28.0	24.7	0.124	36.8	53.9	0.182
$AUC_{0–168h}$	23,021	22,403	182	82,960	63,882	439	35,598	40,164	216
$AUC_{0–168h}/D$	2302	2240	18.2	2765	2129	14.6	3559	4016	21.6
T_{max}	NA	NA	144	NA	NA	24	NA	NA	72

DISCUSSION

BCL-X_L has been a long-standing target for cancer therapy given its demonstrated role in tumor maintenance and drug resistance (*2*, *4*, *5*). The dual BCL-X_L/BCL-2 inhibitors ABT-737 (*43*) and navitoclax (*6*) were the first bone fide inhibitors of the BCL-2 family proteins. These molecules have demonstrated efficacy in numerous preclinical models particularly when combined with specific chemotherapeutic and targeted agents. Thematically, among the most marked combination effects have been noted with microtubule inhibitors such as docetaxel (*16*, *44*) or inhibitors of the MAP kinase (*45*, *46*) signaling pathway. The ability of the dual inhibitors to potentiate anticancer agents within these classes in solid tumor models is primarily mediated by inhibition of BCL-X_L. Since the early demonstration of both clinical efficacy and mechanism-based thrombocytopenia, navitoclax has shown encouraging efficacy in patients with BCL-X_L–dependent cancers such as myelofibrosis and EGFR-mutant lung cancers when combined with ruxolitinib (*13*) or osimertinib (*14*), respectively. While the clinical development of navitoclax continues, the dual inhibitory capacity of this agent inherently confers some limitation to the ability to combine with agents that cause neutropenia given the role of BCL-2 in neutrophil survival (*16*).

Our initial hypothesis was that selective inhibitors of BCL-X_L would have the potential to unlock combinations with anticancer agents that, when dosed concomitantly with navitoclax, have tolerability challenges originating from neutropenia caused by BCL-2 inhibition. Thrombocytopenia resulting from BCL-X_L inhibition would not be avoided by selective SMIs; however, navitoclax trials have demonstrated the ability to manage this toxicity through lead-in dosing and selection of appropriate combination agent (*13*, *14*). However, the unexpected observation that selective BCL-X_L SMIs cause rapid and severe cardiovascular toxicity in preclinical species clearly precluded their further development and demonstrates that the capillary endothelium of the heart and, to a lesser extent, skeletal muscle in higher preclinical species is particularly dependent on BCL-X_L for survival. IL-10 reduction occurred in parallel with platelet depletion, and reduced IL-10 levels may result in a reduced capacity of endothelial cells to resist oxidative stress, possibly contributing to proapoptotic mechanisms (*47*). The cellular origin of increased serum MCP-1, with kinetics approximately inverse to platelet decline, is unclear. MCP-1 is increased during acute myocardial infarction (*28*) and myocarditis (*48*) and has an antiapoptotic function on cardiomyocytes. Our findings support a mechanism of toxicity where cardiac endothelial dysfunction and apoptosis is central, resulting in increased vascular permeability, interstitial myocardial edema, intramyocellular edema, and decreased cardiac output resulting in cardiovascular collapse. Given the complex cross-talk between endothelium and cardiomyocytes (*49*), it is likely that a series of interactions builds over time leading to a loss in cardiomyocyte contractile function.

These findings clearly indicate that selective targeting of BCL-X_L in human patients requires an alternative approach that can spare the cardiovascular system; while the thrombocytopenia that accompanies SMIs may be manageable, identifying a means to increase the TI with respect to this toxicity would be highly beneficial as well. A recent manuscript reported navitoclax-based proteolysis targeting chimeras (PROTACs) that selectively degrade BCL-X_L via

engagement with the E3 ligase cereblon in tumors, while the reported lack of cereblon in platelets allows for preclinical efficacy and reduced thrombocytopenia in tumor-bearing mice (*50*). However, the ability of these molecules to avoid cardiovascular toxicity in dogs or other higher species has not been reported and represents a prerequisite for any further consideration of the PROTAC approach.

To move toward the realization of selective BCL-X_L inhibition in the clinic, we conducted research into whether an ADC approach could deliver an inhibitor selectively to antigen expressing tumor cells, but not normal tissues with a dependency on BCL-X_L. A selection of antigen targets was thus pursued with three primary criteria. The first two criteria pertained to sufficient antigen expression in tumor types that have dependency on BCL-X_L for survival and, second, are relevant to anticancer therapies for which combinations with BCL-X_L inhibitors have shown extensive preclinical rationale and efficacy. The third criterion, which pertains to safety, was the requirement for limited antigen expression on the heart and platelets. A bioinformatics approach led to the identification of several possible antigen targets, from which EGFR was selected on the basis of its fulfillment of these criteria and a clinically validated position in cancer research.

ADC payloads require high functional potency and noninterfering sites for conjugation. Further, as the physicochemical properties of ADCs are sensitive to payload and full drug-linker properties, water solubility of the drug-linker components is a key consideration. As a reflection of the large, hydrophobic, and high-affinity protein-protein interactions, they are designed to disrupt, and BCL-2 family inhibitors present substantial upfront challenges for the generation of ADC payloads. The soluble and nonpermeable payload 10 provided an initial remediation of these challenges, wherein the presence of the tethered sulfonic acid imbued water solubility to an otherwise poorly soluble core (*17*). This enabled smooth conjugation to antibody AM1 via linker technology that had been originally designed for well-behaved auristatin-based drug-linkers. Despite the ability of 10 to confer efficacy in tumor-bearing mice when delivered via AM1-15, the inhibitor in isolation showed negligible impact on dog platelets or cardiovascular tissue following intravenous infusion. These data demonstrated that modulation of permeability properties of BCL-X_L inhibitors could afford robust ADC drug-linkers while increasing the TI of the corresponding ADCs, even in the event of high nonspecific cleavage of the payload in plasma.

The low permeability of payload 10, as defined by highly potent binding and intrinsic potency in permeabilized cells yet reduced potency in intact cells, was a key design feature to mitigate systemic toxicity. The permeabilized cell assay was critical for this effort given the inability to use standard permeability assays with molecules derived from this pharmacophore, a challenge that has plagued other series of BCL-2 family inhibitors (*24*). Unexpectedly, several distinct ADCs having active warhead 10 caused, in monkey kidneys following repeat dosing, mesangial cell hypertrophy while sparing other members of the glomerular triad. This glomerular phenotype has not been previously reported to our knowledge. It is salient in its cellular specificity and atypical phenotype for inhibitors of prosurvival proteins and contrasts with the progressive proximal renal tubular injury and widespread tubular epithelial apoptosis observed with genetic deletion of *bcl2l1* in adult nonhematopoietic tissues (*51*). Although the precise mechanism that drives this ADC-induced phenotype is not clear, the absence of the kidney lesion following administration of the inactive payload-bearing AM1-16 supports a BCL-X_L–mediated effect and underscores the importance of chemical tools for investigating attribution. While no impact on kidney function was observed in the 1-month studies, the accumulation of payload in the kidneys suggested that a progressive effect could manifest over time, ultimately leading to irreversible structural and functional damage within this organ. Alleviating this possibility thus became a requirement for advancing to human clinical trials.

The evidence for accumulation of the low-permeability inhibitor 10 in monkey kidneys following repeat dosing of AM1-15 provided a key insight into how the lesion may be alleviated. Switching from the charged pendant moiety in 10 to the polar yet uncharged side chain in 11 increased functional permeability of the BCL-X_L inhibitor in a manner that still allowed for a sufficient TI with respect to dog cardiovascular safety. However, coupling of 11 with precedented linker 12 afforded a drug-linker (*17*) with poor solubility, thus compromising its utility for further ADC generation. Enabling the use of 11 thus required the generation of unprecedented solubilizing linker and attachment technology that ultimately allowed for the incorporation of semipermeable, yet poorly soluble 11 into the well-behaved drug-linker AAA (*25*) and ultimately ADC AM1-AAA. The demonstration of reduced penetrance and severity of renal toxicity and hematological effects upon repeat dosing of AM1-AAA in monkeys is evidential of effective chemical property modulation. AM1-AAA also demonstrated robust antitumor efficacy in vivo; these data along with additional profiling led to the selection of the AAA drug-linker for clinically directed ADC programs.

While the ADC approach has been successful for natural product–derived cytotoxic agents, platform-based toxicity inherently limits the doses that can be administered (*22*). Targeted payloads that do not indiscriminately target cells have the potential to demonstrate improved TIs, although no examples had been advanced to the clinic at the time of this work. Despite the challenges associated with BCL-2 family inhibitors, the disclosed research indicates that judicious modification of drug-linker properties, as well as the appropriate selection of antibody target, can enable the generation of BCL-X_L–targeting ADCs with suitable properties, efficacy and safety in higher species.

On the basis of the data generated here, we conjugated the AAA drug-linker to a proprietary B7H3-targeting antibody to afford mirzotamab clezutoclax (ABBV-155) (*25*), which recently entered a phase 1 clinical trial. While the results from this study will be reported in due course, the approach described herein has allowed for the first opportunity to selectively target BCL-X_L in patients with cancer and should facilitate multiple additional opportunities for treating patients with BCL-X_L–mediated diseases.

MATERIALS AND METHODS

Antibodies and reagents

Anti-EGFR antibodies AM1 (*36*) and AB033 were generated as previously described. Anti-CD98 antibodies were generated through rodent hybridoma campaign. Briefly, rats and mice were immunized by hock immunizations with a recombinant extracellular domain of human CD98 protein (internally made at AbbVie) as an immunogen. NS0 murine myeloma cells were fused using electrofusion with lymph node cells isolated from immunized animals. Hybridoma clones producing antibodies specific to human and cynomolgus monkey CD98 extracellular domain protein (internally made at

AbbVie) were identified and characterized. The heavy and light chain variable regions corresponding to the anti-CD98 hybridoma antibodies were obtained from hybridoma cells by reverse transcription polymerase chain reaction. The identified variable regions were expressed in mammalian host cells, as chimeric antibodies, in the context of a human immunoglobulin G1 (huIgG1) (L234A and L235A) heavy chain and kappa light chain constant regions, respectively. One of these chimeric antibodies, CL-73023, was used in this study.

Time-resolved fluorescence resonance energy transfer assays

Test compounds were serially diluted in dimethyl sulfoxide (DMSO) starting at 500 μM (20× starting concentration; 100% DMSO), followed by a 1:10 dilution of the compound solution into assay buffer. An aliquot (10 μl) of each compound in 10% DMSO was then transferred into a 384-well plate (#3673, Corning). Then, 10 μl of a 2× protein/probe/antibody mix is added to each well. The final concentrations were 1 nM glutathione *S*-transferase (GST)–BCL-X_L or GST–BCL-2,,100 nM F-Bak [GQVGRQLAIIGDK(6-FAM)INR-amide] probe, and 1 nM for the Tb–anti-GST antibody (*16*, *17*).

The samples were then mixed on a shaker for 1 min and subsequently incubated for 1 hour at room temperature. For each assay plate, a probe/antibody and a protein/antibody/probe mixture were included as a negative and a positive control, respectively. Fluorescence was measured on the Envision (PerkinElmer) using a 340/35-nm excitation filter and 520/525 (F-Bak) and 495/510-nm (Tb-labeled anti-GST antibody) emission filters. Dissociation constants (K_i) were determined using Wang's equation (*52*). The time-resolved fluorescence resonance energy transfer (TR-FRET) assay can be performed in the presence of varying concentrations of human serum to determine apparent median inhibitory concentration after serum protein binding.

Cell viability assay

Molt-4 [American Type Culture Collection (ATCC), Manassas, VA] human acute lymphoblastic leukemia cells or RS4;11 (ATCC, Manassas, VA) human acute lymphoblastic leukemia were plated at 50,000 cells per well in 96-well tissue culture plates in a total volume of 100 μl of tissue culture medium supplemented with 10% human serum (Invitrogen, Carlsbad, CA). Each well was treated with a threefold serial dilution of the compounds of interest from 5 to 0.020 μM. Each concentration was tested in duplicate at least three separate times. The number of viable cells following 48 hours of compound treatment was determined using the CellTiter-Glo luminescent cell viability assay according to the manufacturer's recommendations (Promega Corp., Madison, WI). EC_{50} values were calculated using a sigmoidal fit of the concentration/inhibition response curves using GraphPad Prism 5 (*53*, *54*).

Permeabilized cell JC-1 assay

To determine the effects of compounds independent of their plasma membrane permeability characteristics on mitochondrial membrane potential, a high throughput assay was developed by modifying the procedure of Ryan and Letai (*30*). Briefly, cells were washed and suspended in DTEB buffer [135 mM trehalose, 50 mM KCl, 20 μM EDTA, 20 μM EGTA, 0.1% bovine serum albumin, 5 mM succinate, and 10 mM Hepes-KOH (pH 7.5)] supplemented with 2 μM JC-1 (T4067, Sigma-Aldrich, Saint Louis, MO, USA), 0.01% digitonin (D141, Sigma-Aldrich, Saint Louis, MO, USA), 10 mM β-mercaptoethanol, and oligomycin (20 μg/ml). The cells were incubated at room temperature for 10 min. Afterward, the cells were mixed with equal volume of DTEB buffer and were transferred to a 96-well plate (3915, Corning). Compounds were dispensed along with the negative control DMSO and the positive control carbonyl cyanide *p*-trifluoromethoxyphenylhydrazone (C2920, Sigma-Aldrich, Saint Louis, MO, USA; at 10 μM final for 100% depolarization) using the D300e digital dispenser (Tecan, Baldwin Park, CA). The fluorescence at 590 nm was read every 10 min at 37°C for 1 to 3 hours using a Synergy Neo2 reader (BioTek, Winooski, VT). The compound EC_{50} values based on the % depolarization were calculated using GraphPad program 5 (*53*).

General chemical synthesis procedures

General

^{1}H nuclear magnetic resonance spectra were obtained on a Varian UNITY or Inova (500 MHz), Varian UNITY (400 MHz), or Varian UNITY plus or Mercury (300 MHz) instrument (see the Supplementary Materials for all detailed experimental procedures and data). Chemical shifts are reported as values [in parts per million (ppm)] downfield relative to trimethylsilane (TMS) as an internal standard, with multiplicities reported in the usual manner. Mass spectral analyses were performed on a Finnigan SSQ7000 gas chromatography–mass spectrometry (MS) using different techniques, including electrospray ionization, desorption chemical ionization, and atmospheric pressure chemical ionization, as specified for individual compounds. Exact mass measurements were performed on a Finnigan FTMS Newstar T70 mass spectrometer. The compound is determined to be "consistent" with the chemical formula if the exact mass measurement is within 5.0-ppm relative mass error of the exact monoisotopic mass.

Analytical liquid chromatography–MS (LC-MS) was performed on a Finnigan Navigator mass spectrometer and Agilent 1100 high-performance LC (HPLC) system running Xcalibur 1.2 and Open-Access 1.3 software. The mass spectrometer was operated under positive atmospheric pressure chemical ionization conditions. The HPLC system comprised an Agilent Quaternary pump, degasser, column compartment, autosampler, and diode-array detector, with a Sedere Sedex 75 evaporative light-scattering detector. The column used was a Phenomenex Luna Combi-HTS C8 (2) 5 μm, 100 Å (2.1 mm by 30 mm), using method A or method B, as detailed below. For trifluoroacetic acid method (method A), a gradient of 10 to 100% acetonitrile (solvent 1) and 0.1% trifluoroacetic acid in water (solvent 2) was used, at a flow rate of 2 ml/min (0 to 0.1 min, 10% solvent 1; 0.1 to 2.6 min, 10 to 100% solvent 1; 2.6 to 2.9 min, 100% solvent 1; 2.9 to 3.0 min, 100 to 10% solvent 1). For ammonium acetate method (method B), a gradient of 10 to 100% acetonitrile (solvent 1) and 10 mM NH_4OAc in water (solvent 2) was used, at a flow rate of 1.5 ml/min (0 to 0.1 min, 10% solvent 1; 0.1 to 3.1 min, 10 to 100% solvent 1; 3.1 to 3.9 min, 100% solvent 1; 3.9 to 4.0 min, 100 to 10% solvent 1). All final analogs were >95% pure as determined by these methods.

Preparative reverse-phase HPLC was performed on an automated Gilson HPLC system, using a SymmetryPrep Shield RP18 prep cartridge, 250-mm by 21.20-mm inside diameter, 10 μm, and a flow rate of 25 ml/min; λ = 214, 245 nm; mobile phase A, 0.1% trifluoroacetic acid in water; mobile phase B, acetonitrile, using a linear gradient of 0 to 70% of B over 40 min, unless otherwise stated.

Preparation of ADCs

General procedure 1 for conjugation

A solution of tris(2-carboxyethyl)phosphine (TCEP; 10 mM, 2.5 equivalents, Bond Breaker, Thermo Fisher Scientific) was added to a solution of antibody (~10 mg/ml in phosphate-buffered saline, pH 7.4), gently stirred, and kept at 37°C for 90 min. Six equivalents of a drug-linker dissolved in DMSO was added to the cooled reduced antibody solution and gently mixed. The reaction mixture was incubated at room temperature for 60 min and purified by desalting. After desalting, the resultant ADC solution was filtered through 0.22-μm filter, and the sample was stored at 4°C (*53*, *54*).

General procedure 2 for conjugation

A solution of TCEP (10 mM, 1.3 equivalents, Bond Breaker, Thermo Fisher Scientific) was added to a solution of antibody (~10 mg/ml in phosphate-buffered saline, pH 7.4), gently stirred, and kept at 37°C for 90 min. A total of 3.5 equivalents of a linker drug dissolved in DMSO was added to the cooled reduced antibody solution and gently mixed. The reaction mixture was incubated at room temperature for 60 min and purified by HIC (*53*, *54*). See tables S15 and S16 for specific ADC protocol and observed mass, respectively.

HIC purification (purified DAR2 ADCs)

The sample was loaded onto column packed with Phenyl Sepharose high-performance resin (GE Healthcare). HIC fractions were analyzed by analytical HIC chromatography, and appropriate fractions were pooled, concentrated, and purified by desalting. The resultant ADC solution was then concentrated and filtered.

Hydrolysis (AM1-25-D2)

Purified ADC was hydrolyzed by adding 10% (v/v) of 1 M borate buffer (pH 8.0) and incubated in the dark at room temperature for 48 hours. After hydrolysis, the resultant ADC solution was concentrated and filtered.

DAR determination

DAR determination was done by LC-MS or HIC. LC-MS analysis was performed using an Agilent 1100 HPLC system interfaced to an Agilent LC/mass spectrometry detector (MSD) time-of-flight 6220 electrospray ionization mass spectrometer. The ADC was reduced with 5 mM (final concentration) Bond Breaker TCEP solution (Thermo Fisher Scientific, Rockford, IL), loaded onto a Protein Microtrap (Michrom Bioresources, Auburn, CA) desalting cartridge, and eluted with a gradient of 10% B to 75% B in 0.2 min at ambient temperature. Mobile phase A was H_2O with 0.1% formic acid, mobile phase B was acetonitrile with 0.1% formic acid, and the flow rate was 0.2 ml/min. Electrospray ionization–time-of-flight mass spectra of the coeluting light and heavy chains were acquired using Agilent MassHunter acquisition software. The extracted intensity versus mass/charge ratio spectrum was deconvoluted using the Maximum Entropy feature of MassHunter software to determine the mass of each reduced antibody fragment. DAR was calculated from the deconvoluted spectrum by summing intensities of the naked and modified peaks for the light chain and heavy chain, normalized by multiplying intensity by the number of drugs attached. The summed, normalized intensities were divided by the sum of the intensities, and the summing results for two light chains and two heavy chains produced a final average DAR value for the full ADC. Thiosuccinimide hydrolysis of a bioconjugate can be monitored by electrospray MS since the addition of water to the conjugate results in an increase of 18 Da to the observable molecular weight of the conjugate.

Size exclusion chromatography

Size exclusion chromatography (SEC) was performed using Waters ACQUITY UPLC Protein BEH SEC Column (200 Å, 1.7 μm, 4.6 mm by 150 mm) with 100 mM sodium phosphate, 150 mM sodium chloride, and 10% (v/v) of acetonitrile (pH 7.0) at a flow rate of 0.4 ml/min. The peak area absorbance at 280 nm was determined for each of the high–molecular weight and monomeric eluents by integration of the area under the curve. The % aggregate fraction of the conjugate sample was determined by dividing the peak area absorbance at 280 nm for the high–molecular weight eluent by the sum of the peak area absorbances at 280 mM of the high–molecular weight and monomeric eluents multiplied by 100%. The procedure, DAR, % aggregation, purification and hydrolysis details, and observed mass are listed in tables S15 and S16 (*53*, *54*).

Endotoxin analysis was performed on an Endosafe Nexgen MCS instrument (Charles River) using limulus amebocyte lysate (LAL) cartridges by standard protocol. All materials had endotoxin levels below 1 Eu/mg.

In vivo efficacy experiments

The cell line H1650 was purchased from the ATCC (Manassas, VA) and cell line PC-9 purchased from the European Collection of Authenticated Cell Cultures (Salisbury, UK). H1650 was derived from a pleural effusion of a patient with adenocarcinoma of the lung (NSCLC). PC-9 was derived from a metastatic nodule of a patient with NSCLC. The cells were maintained as monolayer cultures in RPMI 1640 medium (Gibco) supplemented with 10% heat-inactivated fetal bovine serum (Hyclone). Cells were propagated to maximally five passages before inoculation. All cultures were routinely tested and confirmed free of *Mycoplasma* spp. infection using the MycoAlert PLUS Mycoplasma detection kit (Lonza), and cell lines were confirmed free of adventitious agents by IMPACT testing (IDEXX BioAnalytics, Columbia, MO). To generate tumor-bearing mice, 5×10^6 viable cells per mouse were inoculated subcutaneously in the right flank of 8-week-old SCID/bg female mice. Mice were obtained from Charles River (Wilmington, MA). The body weight upon therapy was approximately 22 g. Food and water were available ad libitum. Mice were acclimated to the animal facilities for a period of at least 1 week before commencement of experiments. Animals were tested in the light phase of a 12-hour light:12-hour dark schedule (lights on at 06:00 hours). The injection volume of the tumor cell suspension was 0.2 ml composed of a 1:1 mixture of Spinner Modification of minimum essential Eagle's medium (SMEM) and Matrigel (BD, Franklin Lakes, NJ). Tumors were size-matched by match distribution at a volume of approximately 200 mm^3. Group size was determined by a power analysis using historical data for each individual model so that a 25% effect size would be in a 95% confidence interval. Therapy began 1 day after size matching. Measurements of the length (L) and width (W) of the tumor were blinded and taken via electronic caliper, and the volume was calculated according to the following equation: $V = L \times W^2/2$. Mice were euthanized when tumor volume reached 3000 mm^3 or skin ulcerations occurred. Tumor volume was estimated one to three times weekly. The significance of differences in response amplitude or durability between treatment groups was determined by a Student's t test or Mann-Whitney U test, respectively. Student's t test was used to determine significance between two groups using either vehicle or best single agent as the baseline for significances rather than an analysis of variance (ANOVA), which compares multiple groups.

Mann-Whiney *U* test was used over Student's *t* test for calculating significance for tumor growth delay (TGD) values because the assumptions used to calculate TGD do not allow for Student's *t* test usage (*53*, *54*). No in vivo data were excluded. All experiments were conducted in compliance with AbbVie's Institutional Animal Care and Use Committee under the protocol number 1803D00047 and the National Institutes of Health Guide for Care and Use of Laboratory Animals guidelines in a facility accredited by the Association for the Assessment and Accreditation of Laboratory Animal Care.

IHC in tumor samples

EGFR expression of xenograft models was assessed by immunohistochemical staining using the Dako Pharm Dx kit per the manufacturer's instructions. Paraffin sections (4 μm) were deparaffinized and rehydrated per standard methods, antigen retrieval was performed, and endogenous peroxidase and nonspecific protein binding sites were blocked [peroxidase blocking reagent (S2001, Dako, Carpinteria, CA) and background sniper (BS966G, Biocare, Concord, CA)]. Slides were subsequently incubated in primary antibody for 1 hour at room temperature. The detection system used was EnVision+ polymer for mouse or rabbit with 3, 3′-diaminobenzidine (DAB) as chromogen (#K4007 or #K4011, Dako) and counterstained with hematoxylin (#S3301, Dako). IHC results were evaluated by a board-certified pathologist using the *H*-score scoring paradigm.

Assessment of platelet levels

The influence of BCL-X_L inhibitors on the number of circulating platelets in SCID/bg mice was tested following a single intravenous injection (compound 9, 10, or AM1-15) or oral gavage (navitoclax). Before the administration of vehicle, navitoclax, 9, 10, or AM1-15, the mice were randomly assigned to treatment groups ($N = 15$). At 6, 72, and 168 hours after the administration of drug, five mice were anesthetized by inhalation of sevoflurane, and blood was obtained from puncture of the retro-orbital plexus and collected in heparinized vials. Mice were not allowed to recover from anesthesia and were euthanized (*53*). Platelets were counted in the Advia 2120 hematology analyzer (Siemens Healthineers).

Pharmacokinetic analysis of AM1-15 (purified DAR2 and broad DAR4) in cynomolgus monkeys and representative bioanalytical methods for all ADCs evaluated in monkeys

Serum samples were analyzed using both total and conjugate MSD assays. The TAb assay was used biotinylated LMH-12–anti-806 idiotype for capture and Sulfo-Tag–labeled LMH-12–anti-806 idiotype for electrochemiluminescence detection, while the conjugated antibody assay was used biotinylated anti–BCL-X_L inhibitor (JXS11-50A2) for capture and Sulfo-Tag–labeled LMH-12–anti-806 idiotype for electrochemiluminescence detection. AM1-15 (purified DAR2 or broad DAR4) was used for the standard curves for the respective analyses. In both assays, samples were analyzed at a 1% final serum concentration. Standard curve fitting and data evaluation were performed using XLfit4 software. A calibration curve was plotted from MSD luminescence units versus theoretical standard concentrations. A four-parameter logistic model was used for curve fitting. The regression equation for the calibration curve was then used to back calculate the measured concentrations. Plates passed when at least two-third of the quality controls were within 30% of the expected values. The linear ranges were 0.0244 to 100 μg/ml and 0.0274 to 20 μg/ml for DAR2 and broad DAR4 AM1-15 TAb and conjugated antibody assays, respectively. The lower limits of quantitation were 0.0244 μg/ml (TAb) and 0.0274 μg/ml (conjugated antibody). Values that were below the quantitation limit were treated as 0 when computing mean concentrations and toxicokinetic parameters.

Released concentrations of inhibitor 10 in plasma were determined by HPLC-MS/MS analysis after protein precipitation. The concentrations of study samples were calculated by regression analysis of the peak area ratio (parent/internal standard) of the spiked plasma standards versus concentration. Samples were bracketed with standard curves containing seven standards each, with a range of 0.5 to 200 ng/ml. Quadratic fitting with $1/x^2$ weighting was used to fit the standards, with accuracies between 95.1 and 103.8% of theoretical values. The R^2 value of the fitting was 0.9948, and the lower limit of quantitation was 0.5 ng/ml. Pharmacokinetic parameters were calculated using Phoenix WinNonlin, version 6.3 (Pharsight Corporation, St. Louis, MO) by noncompartmental analysis with NCA Model 200-202 and the linear trapezoidal method. All raw data and the final report are kept on file at AbbVie.

Anesthetized canine experimental protocol

The procedure for evaluating the effects of molecules on cardiovascular parameters in anesthetized dogs was followed from a previous report (*26*). All procedures were approved by AbbVie's Institutional Animal Care and Use Committee and carried out in American Association for Accreditation of Laboratory Animal Care–accredited facilities.

Repeat dose exploratory studies in cynomolgus monkeys

Toxicity of BCL-X_L ADCs was evaluated in non–good laboratory practice (GLP) in one single-dose toxicokinetic/tolerability and four dose range finding studies. In all the non-GLP studies, BCL-X_L ADC was administered intravenously (slow bolus). In the dose range finding studies, standard toxicology end points included clinical signs, body weights, food consumption, toxicokinetics, clinical pathology (hematology, coagulation, clinical chemistry, and urinalysis), and anatomic pathology (organ weights, gross necropsy evaluations, and histopathology). All animal studies were conducted in accordance with the guidelines and protocols established and approved by the internal Institutional Animal Care and Use Committee of AbbVie. All BCL-X_L ADCs administered to cynomolgus monkeys in non-GLP toxicity studies are listed in table S4.

Anti–drug-linker and activated caspase-3 IHC

To generate monoclonal antibodies specifically recognizing BCL-X_L SMI, the BCL-X_L drug-linker 15 conjugated to mariculture keyhole limpet hemocyanin (KLH; Thermo Fisher Scientific, catalog no. 77600) was used as immunogen. SJL female 8- to 10-week-old mice were hock immunized, and hybridomas were generated by e-Fusion of NS0 and lymph node cells isolated from immunized mice. Hybridomas producing antibodies specific for the BCL-X_L drug-linker were identified by enzyme-linked immunosorbent assay against ADC containing the BCL-XL drug-linker 15. A control ADC containing a non–BCL-XL–targeting drug-linker [MCVC–PABC–monomethyl auristatin E (MMAE)] was used for counterscreen to ensure drug-linker specificity. JXS11-50A2 monoclonal antibody was purified from hybridoma supernatant using MabSelect SuRe (GE Healthcare, catalog no. 17543803) column and used for IHC staining at a dilution of 1:10,000. Antigen retrieval was performed using Dako Proteinase

K (S3020) for 5 min, followed by peroxide block (Biocare, PX968) for 5 min, BCL-X_L antibody for 60 min, horseradish peroxidase–labeled polymer (Dako, K4001) for 30 min, DAB (Biocare, IPK5010) for 5 min, and hematoxylin (Biocare, IPCS5006) for 5 min. Activated caspase-3 was detected in rehydrated paraffin sections following 20 min of antigen retrieval, peroxidase inactivation, avidin and biotin blocking, and detection with Cell Signaling Technology (Danvers, MA) rabbit anti–activated caspase-3 (#9661S) at 1:100 for 1 hour at ambient temperature. Goat anti-rabbit (1:200) peroxidase secondary was detected with Vector Labs (Temecula, CA) ABC reagent and then DAB substrate for 4 min with hematoxylin counterstaining.

Electron microscopy

The heart and kidney were processed and embedded in epoxy resin. Ultrathin sections were stained with 2% methanolic uranyl acetate, followed by Reynolds' lead citrate and examination on a JEOL JEM-1400 microscope (JEOL, Boston, MA) and AMT XR41 digital camera.

Supplementary Materials

This PDF file includes:

Supplementary Text
Chemical Structures 1 to 15
Figs. S1 to S5
Tables S1 to S17
References

REFERENCES AND NOTES

1. D. Hanahan, R. A. Weinberg, Hallmarks of cancer: The next generation. *Cell* **144**, 646–674 (2011).
2. A. Frenzel, F. Grespi, W. Chmelewskij, A. Villunger, Bcl2 family proteins in carcinogenesis and the treatment of cancer. *Apoptosis* **14**, 584–596 (2009).
3. N. Khan, B. Kahl, Targeting BCL-2 in hematologic malignancies. *Target. Oncol.* **13**, 257–267 (2018).
4. S. A. Amundson, T. G. Myers, D. Scudiero, S. Kitada, J. C. Reed, A. J. Fornace Jr., An informatics approach identifying markers of chemosensitivity in human cancer cell lines. *Cancer Res.* **60**, 6101–6110 (2000).
5. M. Vogler, Targeting BCL2-proteins for the treatment of solid tumours. *J. Adv. Med.* **2014**, 1–14 (2014).
6. C. Tse, A. R. Shoemaker, J. Adickes, M. G. Anderson, J. Chen, S. Jin, E. F. Johnson, K. C. Marsh, M. J. Mitten, P. Nimmer, L. Roberts, S. K. Tahir, Y. Xiao, X. Yang, H. Zhang, S. Fesik, S. H. Rosenberg, S. W. Elmore, ABT-263: A potent and orally bioavailable Bcl-2 family inhibitor. *Cancer Res.* **68**, 3421–3428 (2008).
7. C. M. Park, M. Bruncko, J. Adickes, J. Bauch, H. Ding, A. Kunzer, K. C. Marsh, P. Nimmer, A. R. Shoemaker, X. Song, S. K. Tahir, C. Tse, X. Wang, M. D. Wendt, X. Yang, H. Zhang, S. W. Fesik, S. H. Rosenberg, S. W. Elmore, Discovery of an orally bioavailable small molecule inhibitor of prosurvival B-cell lymphoma 2 proteins. *J. Med. Chem.* **51**, 6902–6915 (2008).
8. A. W. Roberts, J. F. Seymour, J. R. Brown, W. G. Wierda, T. J. Kipps, S. L. Khaw, D. A. Carney, S. Z. He, D. C. S. Huang, H. Xiong, Y. Cui, T. A. Busman, E. M. McKeegan, A. P. Krivoshik, S. H. Enschede, R. Humerickhouse, Substantial susceptibility of chronic lymphocytic leukemia to BCL2 inhibition: Results of a phase I study of navitoclax in patients with relapsed or refractory disease. *J. Clin. Oncol.* **30**, 488–496 (2012).
9. T. J. Kipps, H. Eradat, S. Grosicki, J. Catalano, W. Cosolo, I. S. Dyagil, S. Yalamanchili, A. Chai, S. Sahasranaman, E. Punnoose, D. Hurst, H. Pylypenko, A phase 2 study of the BH3 mimetic BCL2 inhibitor navitoclax (ABT-263) with or without rituximab, in previously untreated B-cell chronic lymphocytic leukemia. *Leuk. Lymphoma* **56**, 2826–2833 (2015).
10. H. Zhang, P. M. Nimmer, S. K. Tahir, J. Chen, R. M. Fryer, K. R. Hahn, L. A. Iciek, S. J. Morgan, M. C. Nasarre, R. Nelson, L. C. Preusser, G. A. Reinhart, M. L. Smith, S. H. Rosenberg, S. W. Elmore, C. Tse, Bcl-2 family proteins are essential for platelet survival. *Cell Death Differ.* **14**, 943–951 (2007).
11. L. Gandhi, D. R. Camidge, M. R. de Oliveira, P. Bonomi, D. Gandara, D. Khaira, C. L. Hann, E. M. McKeegan, E. Litvinovich, P. M. Hemken, C. Dive, S. H. Enschede, C. Nolan, Y. L. Chiu, T. Busman, H. Xiong, A. P. Krivoshik, R. Humerickhouse, G. I. Shapiro, C. M. Rudin, Phase I study of navitoclax (ABT-263), a novel Bcl-2 family inhibitor, in patients with small-cell lung cancer and other solid tumors. *J. Clin. Oncol.* **29**, 909–916 (2011).
12. A. J. Souers, J. D. Leverson, E. R. Boghaert, S. L. Ackler, N. D. Catron, J. Chen, B. D. Dayton, H. Ding, S. H. Enschede, W. J. Fairbrother, D. C. S. Huang, S. G. Hymowitz, S. Jin, S. L. Khaw, P. J. Kovar, L. T. Lam, J. Lee, H. L. Maecker, K. C. Marsh, K. D. Mason, M. J. Mitten, P. M. Nimmer, A. Oleksijew, C. H. Park, C. M. Park, D. C. Phillips, A. W. Roberts, D. Sampath, J. F. Seymour, M. L. Smith, G. M. Sullivan, S. K. Tahir, C. Tse, M. D. Wendt, Y. Xiao, J. C. Xue, H. Zhang, R. A. Humerickhouse, S. H. Rosenberg, S. W. Elmore, ABT-199, a potent and selective BCL-2 inhibitor, achieves antitumor activity while sparing platelets. *Nat. Med.* **19**, 202–208 (2013).
13. C. N. Harrison, J. S. Garcia, R. A. Mesa, T. C. P. Somervaille, R. S. Komrokji, N. Pemmaraju, C. Jamieson, N. Papadantonakis, J. M. Foran, C. L. O'Connell, L. Holes, J. Jia, J. Harb, J. Hutti, J. T. Prchal, Results from a phase 2 study of navitoclax in combination with ruxolitinib in patients with primary or secondary myelofibrosis. *Blood* **134** (Suppl. 1), 671 (2019).
14. E. M. Bertino, R. D. Gentzler, S. Clifford, J. Kolesar, A. Muzikansky, E. B. Haura, Z. Piotrowska, D. R. Camidge, T. E. Stinchcombe, C. Hann, J. Malhotra, L. C. Villaruz, C. P. Paweletz, C. L. Lau, L. Sholl, N. Takebe, J. A. Moscow, G. I. Shapiro, P. A. Jänne, G. R. Oxnard, Phase IB study of osimertinib in combination with navitoclax in EGFR-mutant NSCLC following resistance to initial EGFR therapy (ETCTN 9903). *Clin. Cancer Res.* **27**, 1604–1611 (2021).
15. M. Puglisi, L. R. Molife, M. J. de Jonge, K. H. Khan, L. van Doorn, M. D. Forster, M. Blanco, M. Gutierrez, C. Franklin, T. Busman, J. Yang, F. A. Eskens, Phase I safety and pharmacokinetic (PK) study of navitoclax (N) in combination with docetaxel (D) in patients (pts) with solid tumors. *J. Clin. Oncol.* **29**, 2518 (2011).
16. J. D. Leverson, D. C. Phillips, M. J. Mitten, E. R. Boghaert, D. Diaz, S. K. Tahir, L. D. Belmont, P. Nimmer, Y. Xiao, X. M. Ma, K. N. Lowes, P. Kovar, J. Chen, S. Jin, M. Smith, J. Xue, H. Zhang, A. Oleksijew, T. J. Magoc, K. S. Vaidya, D. H. Albert, J. M. Tarrant, N. La, L. Wang, Z. F. Tao, M. D. Wendt, D. Sampath, S. H. Rosenberg, C. Tse, D. C. S. Huang, W. J. Fairbrother, S. W. Elmore, A. J. Souers, Exploiting selective BCL-2 family inhibitors to dissect cell survival dependencies and define improved strategies for cancer therapy. *Sci. Transl. Med.* **7**, 279ra40 (2015).
17. L. Wang, G. A. Doherty, A. S. Judd, Z. F. Tao, T. M. Hansen, R. R. Frey, X. Song, M. Bruncko, A. R. Kunzer, X. Wang, M. D. Wendt, J. A. Flygare, N. D. Catron, R. A. Judge, C. H. Park, S. Shekhar, D. C. Phillips, P. Nimmer, M. L. Smith, S. K. Tahir, Y. Xiao, J. Xue, H. Zhang, P. N. Le, M. J. Mitten, E. R. Boghaert, W. Gao, P. Kovar, E. F. Choo, D. Diaz, W. J. Fairbrother, S. W. Elmore, D. Sampath, J. D. Leverson, A. J. Souers, Discovery of A-1331852, a first-in-class, potent and orally-bioavailable BCL-X_L inhibitor. *ACS Med. Chem. Lett.* **11**, 1829–1836 (2020).
18. H. Xiong, R. S. Pradhan, A. Nada, A. P. Krivoshik, K. D. Holen, J. W. Rhodes, G. B. Gordon, R. Humerickhouse, W. M. Awni, Studying navitoclax, a targeted anticancer drug, in healthy volunteers—Ethical considerations and risk/benefit assessments and management. *Anticancer Res* **34**, 3739–3746 (2014).
19. P. Khongorzul, C. J. Ling, F. U. Khan, A. U. Ihsan, J. Zhang, Antibody-drug conjugates: A comprehensive review. *Mol. Cancer Res.* **18**, 3–19 (2020).
20. S. Coats, M. Williams, B. Kebble, R. Dixit, L. Tseng, N. S. Yao, D. A. Tice, J. C. Soria, Antibody-drug conjugates: Future directions in clinical and translational strategies to improve the therapeutic index. *Clin. Cancer Res.* **25**, 5441–5448 (2019).
21. J. C. Masters, D. J. Nickens, D. Xuan, R. L. Shazer, M. Amantea, Clinical toxicity of antibody drug conjugates: A meta-analysis of payloads. *Invest. New Drugs* **36**, 121–135 (2018).
22. A. Wolska-Washer, T. Robak, Safety and tolerability of antibody-drug conjugates in cancer. *Drug Saf.* **42**, 295–314 (2019).
23. Y. J. Wang, Y. Y. Li, X. Y. Liu, X. L. Lu, X. Cao, B. H. Jiao, Marine antibody-drug conjugates: Design strategies and research progress. *Mar. Drugs* **15**, 18 (2017).
24. W. J. Fairbrother, J. D. Leverson, D. Sampath, A. J. Souers, Discovery and development of venetoclax, a selective antagonist of BCL-2. *Success. Drug Discov.* **4**, 225–245 (2019).
25. A. W. Tolcher, B. A. Carneiro, A. Dowlati, A. Ryan, A. Razak, Y. K. Chae, J. A. Villella, S. Coppola, S. Englert, A. C. Phillips, A. J. Souers, Z. Salman, S. Penugonda, J. D. Powderly, P. LoRusso, A first-in-human study of mirzotamab clezutoclax as monotherapy and in combination with taxane therapy in relapsed/refractory solid tumors: Dose escalation results. *J. Clin. Oncol.* **39**, 15 (2021).
26. Y. E. Koshman, A. S. Wilsey, B. M. Bird, A. L. Endemann, S. Sadilek, J. Treadway, R. L. Martin, J. S. Polakowski, G. A. Gintant, S. W. Mittelstadt, Drug-induced QT prolongation: Concordance of preclinical anesthetized canine model in relation to published clinical observations for ten CiPA drugs. *J. Pharmacol. Toxicol. Methods* **103**, 106871 (2020).
27. K. S. Weber, P. J. Nelson, H. J. Gröne, C. Weber, Expression of CCR2 by endothelial cells: Implications for MCP-1 mediated wound injury repair and In vivo inflammatory activation of endothelium. *Arterioscler. Thromb. Vasc. Biol.* **19**, 2085–2093 (1999).
28. H. Morimoto, M. Takahashi, Role of monocyte chemoattractant protein-1 in myocardial infarction. *Int. J. Biomed. Sci.* **3**, 159–167 (2007).
29. Z. F. Tao, X. Wang, J. Chen, J. P. Ingram, S. Jin, R. A. Judge, P. J. Kovar, C. Park, C. Sun, B. D. Wakefield, L. Zhou, H. Zhang, S. W. Elmore, D. C. Phillips, A. S. Judd, J. D. Leverson,

A. J. Souers, Structure-based design of A-1293102, a potent and selective BCL-XL inhibitor. *ACS Med. Chem. Lett.* **12**, 1011–1016 (2021).
30. J. Ryan, A. Letai, BH3 profiling in whole cells by fluorimeter or FACS. *Methods* **61**, 156–164 (2013).
31. P. Senter, E. Sievers, The discovery and development of brentuximab vedotin for use in relapsed Hodgkin lymphoma and systemic anaplastic large cell lymphoma. *Nat. Biotechnol.* **30**, 631–637 (2012).
32. K. R. Durbin, C. Phipps, X. Liao, Mechanistic modeling of antibody-drug conjugate internalization at the cellular level reveals inefficient processing steps. *Mol. Cancer Ther.* **17**, 1341–1351 (2018).
33. L. Mazzarella, A. GuidA, G. Curigliano, Cetuximab for treating non-small cell lung cancer. *Expert Opin. Biol. Ther.* **18**, 483–493 (2018).
34. G. Lessene, P. E. Czabotar, B. E. Sleebs, K. Zobel, K. N. Lowes, J. M. Adams, J. B. Baell, P. M. Colman, K. Deshayes, W. J. Fairbrother, J. A. Flygare, P. Gibbons, W. J. A. Kersten, S. Kulasegaram, R. M. Moss, J. P. Parisot, B. J. Smith, I. P. Street, H. Yang, D. C. S. Huang, K. G. Watson, Structure-guided design of a selective BCL-X_L inhibitor. *Nat. Chem. Biol.* **9**, 390–397 (2013).
35. A. E. Fouts, L. Comps-Agrar, K. F. Stengel, D. Ellerman, A. J. Schoeffler, S. Warming, D. L. Eaton, B. Feierbach, Mechanism for neutralizing activity by the anti-CMV gH/gL monoclonal antibody MSL-109. *Proc. Natl. Acad. Sci. U.S.A.* **111**, 8209–8214 (2014).
36. A. C. Phillips, E. R. Boghaert, K. S. Vaidya, H. D. Falls, M. J. Mitten, P. J. DeVries, L. Benatuil, C. M. Hsieh, J. A. Meulbroek, S. C. Panchal, F. G. Buchanan, K. R. Durbin, M. J. Voorbach, D. R. Reuter, S. R. Mudd, L. I. Loberg, S. L. Ralston, D. Cao, H. K. Gan, A. M. Scott, E. B. Reilly, Characterization of ABBV-221, a tumor-selective EGFR-targeting antibody drug conjugate. *Mol. Cancer Ther.* **17**, 795–805 (2018).
37. I. E. Wertz, S. Kusam, C. Lam, T. Okamoto, W. Sandoval, D. J. Anderson, E. Helgason, J. A. Ernst, M. Eby, J. Liu, L. D. Belmont, J. S. Kaminker, K. M. O'Rourke, K. Pujara, P. B. Kohli, A. R. Johnson, M. L. Chiu, J. R. Lill, P. K. Jackson, W. J. Fairbrother, S. Seshagiri, M. J. C. Ludlam, K. G. Leong, E. C. Dueber, H. Maecker, D. C. S. Huang, V. M. Dixit, Sensitivity to antitubulin chemotherapeutics is regulated by MCL1 and FBW7. *Nature* **471**, 110–114 (2011).
38. "Common terminology criteria for adverse events (CTCAE)"; https://ctep.cancer.gov/protocolDevelopment/electronic_applications/ctc.htm [accessed 23 May 2023].
39. J. L. Rojko, M. G. Evans, S. A. Price, B. Han, G. Waine, M. DeWitte, J. Haynes, B. Freimark, P. Martin, J. T. Raymond, W. Evering, M. C. Rebelatto, E. Schenck, C. Horvath, Formation, clearance, deposition, pathogenicity, and identification of biopharmaceutical-related immune complexes: Review and case studies. *Toxicol. Pathol.* **42**, 725–764 (2014).
40. L. Boysen, B. M. Viuff, L. H. Landsy, J. Lykkesfeldt, J. T. Raymond, S. A. Price, H. Pelzer, B. Lauritzen, Formation and glomerular deposition of immune complexes in mice administered human antibodies: Evaluation of dose, frequency, and biomarkers. *Toxicol. Pathol.* **48**, 570–585 (2020).
41. G. M. Hayes, L. Chinn, J. M. Cantor, B. Cairns, Z. Levashova, H. Tran, T. Velilla, D. Duey, J. Lippincott, J. Zachwieja, M. H. Ginsberg, E. H. van der Horst, Antitumor activity of an anti-CD98 antibody. *Int. J. Cancer* **137**, 710–720 (2015).
42. D. F. Veber, S. R. Johnson, H. Y. Cheng, B. R. Smith, K. W. Ward, K. D. Kopple, Molecular properties that influence the oral bioavailability of drug candidates. *J. Med. Chem.* **45**, 2615–2623 (2002).
43. T. Oltersdorf, S. W. Elmore, A. R. Shoemaker, R. C. Armstrong, D. J. Augeri, B. A. Belli, M. Bruncko, T. L. Deckwerth, J. Dinges, P. J. Hajduk, M. K. Joseph, S. Kitada, S. J. Korsmeyer, A. R. Kunzer, A. Letai, C. Li, M. J. Mitten, D. G. Nettesheim, S. Ng, P. M. Nimmer, J. M. O'Connor, A. Oleksijew, A. M. Petros, J. C. Reed, W. Shen, S. K. Tahir, C. B. Thompson, K. J. Tomaselli, B. Wang, M. D. Wendt, H. Zhang, S. W. Fesik, S. H. Rosenberg, An inhibitor of Bcl-2 family proteins induces regression of solid tumours. *Nature.* **435**, 677–681 (2005).
44. N. Tan, M. Malek, J. Zha, P. Yue, R. Kassees, L. Berry, W. J. Fairbrother, D. Sampath, L. D. Belmont, Navitoclax enhances the efficacy of taxanes in non-small cell lung cancer models. *Clin. Cancer Res.* **17**, 1394–1404 (2010).
45. J. Chen, S. Jin, V. Abraham, X. Huang, B. Liu, M. J. Mitten, P. Nimmer, X. Lin, M. Smith, Y. Shen, A. R. Shoemaker, S. K. Tahir, H. Zhang, S. L. Ackler, S. H. Rosenberg, H. Maecker, D. Sampath, J. D. Leverson, C. Tse, S. W. Elmore, The Bcl-2/Bcl-X_L/Bcl-w inhibitor, navitoclax, enhances the activity of chemotherapeutic agents in vitro and in vivo. *Mol. Cancer Ther.* **10**, 2340–2349 (2011).
46. R. B. Corcoran, K. A. Cheng, A. N. Hata, A. C. Faber, H. Ebi, E. M. Coffee, P. Greninger, R. D. Brown, J. T. Godfrey, T. J. Cohoon, Y. Song, E. Lifshits, K. E. Hung, T. Shioda, D. Dias-Santagata, A. Singh, J. Settleman, C. H. Benes, M. Mino-Kenudson, K. Wong, J. A. Engelman, Synthetic lethal interaction of combined BCL-XL and MEK inhibition promotes tumor regressions in KRAS mutant cancer models. *Cancer Cell* **23**, 121–128 (2013).
47. M. G. Scioli, G. Storti, F. D'Amico, R. R. Guzmán, F. Centofanti, E. Doldo, E. M. C. Miranda, A. Orlandi, Oxidative stress and new pathogenetic mechanisms in endothelial dysfunction: Potential diagnostic biomarkers and therapeutic Targets. *J. Clin. Med.* **9**, 1995 (2020).
48. S. Göser, R. Ottl, A. Brodner, T. J. Dengler, J. Torzewski, K. Egashira, N. R. Rose, H. A. Katus, Z. Kaya, Critical role for monocyte chemoattractant protein-1 and macrophage inflammatory protein-1alpha in induction of experimental autoimmune myocarditis and effective anti-monocyte chemoattractant protein-1 gene therapy. *Circulation* **112**, 3400–3407 (2005).
49. J. Noireaud, R. Andriantsitohaina, Recent insights in the paracrine modulation of cardiomyocyte contractility by cardiac endothelial cells. *Biomed. Res. Int.* **2014**, 923805 (2014).
50. S. Khan, X. Zhang, D. Lv, Q. Zhang, Y. He, P. Zhang, X. Liu, D. Thummuri, Y. Yuan, J. S. Wiegand, J. Pei, W. Zhang, A. Sharma, C. R. McCurdy, V. M. Kuruvilla, N. Baran, A. A. Ferrando, Y. Kim, A. Rogojina, P. J. Houghton, G. Huang, R. Hromas, M. Konopleva, G. Zheng, D. Zhou, A selective BCL-X_L PROTAC degrader achieves safe and potent antitumor activity. *Nat. Med.* **25**, 1938–1947 (2019).
51. K. Brinkmann, P. Waring, S. P. Glaser, V. Wimmer, D. L. Cottle, M. S. Tham, D. Nhu, L. Whitehead, A. R. Delbridge, G. Lessene, I. M. Smyth, M. J. Herold, G. L. Kelly, S. Grabow, A. Strasser, BCL-XL exerts a protective role against anemia caused by radiation-induced kidney damage. *EMBO J.* **39**, e105561 (2020).
52. Z. X. Wang, An exact mathematical expression for describing competitive binding of two different ligands to a protein molecule. *FEBS Lett.* **360**, 111–114 (1995).
53. S. L. Ackler, N. B. Bennett, E. R. Boghaert, S. C. Cullen, G. Doherty, R. R. Frey, A. R. Haight, A. S. Judd, A. R. Kunzer, V. L. Marin, X. Shen, X. Song, A. J. Souers, G. M. Sullivan, Z. Tao, X. Wang, D. S. Welch, M. D. Wendt, BCL-XL inhibitory compounds having low cell permeability and antibody drug conjugates including the same. US2016339117A1 (2016).
54. L. Benatuil, M. Bruncko, A. S. Judd, Y. Li, A. Mccluskey, A. C. Phillips, D. C. Phillips, J. Seagal, A. J. Souers, Anti-CD98 antibodies and antibody drug conjugates. WO2017214458 (2017).
55. C. Vonrhein, C. Flensburg, P. Keller, A. Sharff, O. Smart, W. Paciorek, T. Womack, G. Bricogne, Data processing and analysis with the autoPROC toolbox. *Acta Crystallogr. D Biol. Crystallogr.* **67**, 293–302 (2011).
56. A. Vagin, A. Teplyakov, MOLREP: An automated program for molecular replacement. *J. Appl. Cryst.* **30**, 1022–1025 (1997).
57. M. D. Winn, C. C. Ballard, K. D. Cowtan, E. J. Dodson, P. Emsley, P. R. Evans, R. M. Keegan, E. B. Krissinel, A. G. W. Leslie, A. McCoy, S. J. McNicholas, G. N. Murshudov, N. S. Pannu, E. A. Potterton, H. R. Powell, R. J. Read, A. Vagin, K. S. Wilson, Overview of the CCP4 suite and current developments. *Acta Crystallogr. D Biol. Crystallogr.* **67** (Pt. 4), 235–242 (2011).
58. P. Emsley, B. Lohkamp, W. G. Scott, K. Cowtan, Features and development of Coot. *Acta Crystallogr. D Biol. Crystallogr.* **66** (Pt. 4), 486–501 (2010).
59. G. N. Murshudov, P. Skubák, A. A. Lebedev, N. S. Pannu, R. A. Steiner, R. A. Nicholls, M. D. Winn, F. Long, A. A. Vagin, REFMAC5 for the refinement of macromolecular crystal structures. *Acta Crystallogr. D Biol. Crystallogr.* **67** (Pt. 4), 355–367 (2011).
60. G. Bricogne, E. Blanc, M. T. Brandl, C. Flensburg, P Keller, W. Paciorek, P. Roversi, A. Sharff, O. S. Smart, C. Vonrhein. BUSTER, Version 2.10.0, Global Phasing Ltd. (2011).

Acknowledgments: We thank AbbVie employees D. Welch, S. Cullen, and N. Bennet for synthetic chemistry advice; J. Seagal (AbbVie) for generation of CD98 antibodies and BCL-XL SMI antibodies; S. Ngadiman (AbbVie) and J. Clarin (AbbVie) for IHC staining of tumor xenograft samples; L. Miesbauer (AbbVie) for analytical support; J. Harlan (AbbVie) for conjugation advice; and the late G. Sullivan (former AbbVie employee) for conception, chemistry support, and innovations. X-ray diffraction data were collected at beamline 17-ID in the facilities of the Industrial Macromolecular Crystallography Association Collaborative Access Team (IMCA-CAT) at the Advanced Photon Source. These facilities are supported by the companies of the Industrial Macromolecular Crystallography Association. Use of the Advanced Photon Source, an Office of Science User Facility is operated for the US Department of Energy (DOE) Office of Science by Argonne National Laboratory. **Funding:** This work was supported by AbbVie. **Author contributions:** Conceptualization: A.S.J., B.B., W.R.B., A.P., J.D.L., E.R.B., and A.J.S. Methodology: Z.-F.T., Y.L., M.B., N.C., G.D., B.E., A.R.H., T.A.H., G.J.J., R.L.M., S.M., D.C.P., S.L.R., and J.C.K. Investigation: M.J.M., K.R.D., R.F., D.H., S.H., J.H., K.I., R.A.J., A.K., D.M., L.N., P.N., J.P., R.P., X.Sh., X.So., K.R.V., X.W., J.W., Y.X., H.Z., and X.Z. Formal analysis: A.J.S., S.H.R., E.A.B., B.B., and A.P. Visualization: A.J.S., B.B., W.R.B., and R.A.J. Supervision: A.J.S., S.H.R., E.A.B., and S.L.R. Writing—original draft: A.S.J., A.J.S., B.B., W.R.B., D.C.P., J.K.C., A.P., and E.R.B. Writing—review and editing: A.S.J., A.J.S., B.B., W.R.B., D.C.P., J.K.C., A.P., E.R.B., S.H.R., E.A.B., S.L.R., B.E., and N.C. **Competing interests:** All authors are employed by AbbVie or were employed by AbbVie at the time of this work and may own AbbVie stock. M.B., A.S.J., A.C.P., and A.J.S. are inventors and contributors of the granted patent titled "Anti-b7-h3 antibodies and antibody drug conjugates" (WO2017214335A1). E.R.B., A.J.S, A.C.P, A.S.J., and M.B. are inventors and contributors of the granted patent titled "Anti-egfr antibody drug conjugates" (WO2017214282A1). **Data and materials availability:** All data needed to evaluate the conclusions in the paper are present in the paper and/or the Supplementary Materials. The atomic coordinates and structure factors for the various structures have been deposited into the Protein Data Bank and are available under accession number 9AQZ.

Submitted 17 February 2024
Accepted 30 August 2024
Published 4 October 2024
10.1126/sciadv.ado7120